Electronic Supplementary Information (ESI)

Deciphering the bridge oxygen vacancy-induced cascading charge effect for electrochemical ammonia synthesis

Ashmita Biswas, †[a] Narad Barman, †[b] Avinash Nambron, [a] Ranjit Thapa, [b, c] Ramendra Sundar Dey*[a]

[a] *Institute of Nano Science and Technology, Sector-81, Mohali-140306, Punjab, India. E-mail: rsdey@inst.ac.in.*

[b] *Department of Physics, SRM University- Amaravati, Andhra Pradesh-522240, India.*

[c] *Centre for Computational and Integrative Sciences, SRM University- Amaravati, Andhra Pradesh-522240, India.*

† These authors contributed equally.

Experimental section

Chemicals and Materials. Tin chloride pentahydrate ($SnCl_4.5H_2O$), sodium sulfate (Na_2SO_4), ammonium chloride (NH_4Cl), hydrazine monohydrate ($N_2H_4 \cdot H_2O$), para-(dimethylamino) benzaldehyde, potassium hydroxide (KOH), sodium hydroxide (NaOH), trisodium citrate, sodium hypochlorite (NaClO), phenol, and sodium nitroferricyanide ($Na_2[Fe(NO)(CN)_5]$) and dimethyl sulfoxide- d^6 (DMSO-d^6) were all purchased from Sigma Aldrich. Ethanol, hydrochloric acid, sulphuric acid were purchased from Merck India, Carbon cloth was purchased from Kanopy, India and graphite strips were purchased from Excel Instruments. All the aqueous solutions were prepared in DI water and all the chemicals were used without further purification. $^{14}N_2$ cylinder was purchased from Sigma gases and $^{15}N_2$ gas cylinder was purchased from Sigma Aldrich.

Material Characterizations. X-ray diffraction (**XRD**) study of synthesized catalysts was performed on a Bruker D8 advances instrument using Cu-Kα (λ = 1.5406 Å) radiation in the 2θ range from 10° to 80° and slow scan range 25° to 35° with an acceleration voltage of 40 kV. The surface morphological characterization and the presence of various elements in Mo/Ag_3PO_4-10 and Ag_3PO_4 catalysts were investigated using field emission scanning electron microscopy (**FESEM**) and high-resolution transmission electron microscopy (**HRTEM**) analysis, which were carried out on JEOL JSM-7600F and JEM2100 instruments. The surface elemental composition and bonding configuration of the prepared samples was determined using X-ray photoelectron spectroscopy (**XPS**) spectrometer (K-Alpha plus) instruments in an ultrahigh vacuum chamber ($7x10^{-9}$ torr) using Al-Kα radiation (1486.6 eV). **Raman spectroscopy** was performed in a Raman confocal microscope (WITEC Focus innovation Alpha-300) with a 532 nm excitation wavelength. **UV-vis** characterizations were performed in UV-vis-NIR (Cary 5000 UV-vis-NIR, Model: G9825A CARY) spectrophotometer that has the ability to measure 300-2800 nm by a Pb Smart NIR detector. A more precise analysis of the produced ammonia was determined with ^1H nuclear magnetic resonance **(NMR)** measurements in a 400 MHz Bruker Avance II 400 NMR spectrometer. Fourier transform infra-red (**FTIR**) spectroscopy and in-situ **FTIR** were performed in ATR mode as performed on a Bruker Alpha FTIR spectrometer in the range from 500 to 4000 cm^{-1} at room temperature. For FTIR, ZnSe crystal and for in-situ studies Si-face angle crystal (FAC) was used respectively. In order to detect the presence or absence of nitrogenous contamination in the feeding $^{14}N_2$ gas, ion chromatography (**IC**) was performed with Eco IC Metrohm, where the anionic column consisted of Metrosep A Supp 17 – 250/4.0 and the eluent consists of 5 mmol/L Na_2CO_3 and 0.2 mmol/L

Na_2HCO_3 with a flow rate of 0.6 mL/min. All the **pH** measurements were done using the Eutech pH meter instrument. All the electrochemical measurements were performed in CHI 760E and BioLogic VSP potentiostats.

N_2 gas purification. The $^{14}N_2$ gas, commercially purchased from Sigma Aldrich was successively passed through acid (0.05 M H_2SO_4) and alkaline (0.1 M KOH) traps to remove possible contaminants. It is expected that the adventitious NH_3 will get trapped in the acid trap while the base trap would capture NO_x impurities. A detailed analysis of the NH_3 and NO_x impurities in the gas was checked with UV-vis spectroscopic methods.

Determination of NO_x contamination in feeding gas and the working electrolyte. NO_x contamination was determined using the N-(-1-naphthyl)- ethylenediamine dihydrochloride spectrophotometric method. The chromogenic agent was obtained by dissolving sulfanilic acid (0.5 g) in deionized water (90 ml) and acetic acid (5 ml), followed by adding N-(1-naphthyl)-ethylenediamine dihydrochloride (5 mg) and bringing the solution to 100 ml. The prepared solution was covered and protected from light. The chromogenic agent (4 mL) was mixed with 1 mL of the investigating solutions. After an incubation period of 15 min, the absorption spectrum was measured using an ultraviolet-visible spectrophotometer at ~ 540 nm.

Electrochemical N_2 reduction measurements. In this work, all the electrochemical experiments were carried out in an H-type electrolysis cell where the cathodic and anodic compartments were separated by Nafion (115) membrane. This membrane allows the permeability of protons from one chamber to the other and is non-selective to any other ions. The membrane was pre-treated by heating it in 5 wt% H_2O_2 aqueous solution at 80 °C for 1 h and then in ultrapure water at 80 °C for another 1 h. All the measurements were done at room temperature in a three-electrode setup where Pt wire was taken as the counter electrode, Ag/AgCl (3 M KCl) as the reference electrode, and the developed catalysts drop casted on graphite plate as the working electrode (for the ease of post-stability material characterizations, NRR was accomplished on sample modified activated carbon cloth as working electrode). The cell chambers were immersed with the working electrolyte 0.1 M Na_2SO_4. The reference electrode was calibrated concerning the reversible hydrogen electrode (RHE) and their potentials were related by the formula as follows:

$E_{RHE} = E_{Ag/AgCl} + (0.0591 \times pH) + 0.210$ (E^0 at Ag/AgCl, 3 M KCl)

(1)

Prior to each electrolysis, the electrolyte in the cathode compartment was continuously fed with pure Ar and N_2 (99.99 % purity) gases for 30 min each using properly positioned spargers so that the whole cathode was hit by the gas bubbles. All presented polarization curves were steady-state ones after 10 cycles and were measured at 10 mV s^{-1} scan rate and the current density values were normalized to geometric surface areas. Chronoamperometric (CA) tests were conducted in the N_2-saturated 0.1 M Na_2SO_4 solution for 1 h over the potential range from -0.1 to - 0.5 V vs RHE. After each CA test, a measured amount of aliquot was taken out from the electrolyte and studied by indophenol blue and Watt and Chrisp methods for the qualitative detection of ammonia and hydrazine, respectively. Each time an in-line acid trap of the cathode chamber filled with the electrolyte was set to avoid volatilization of the produced ammonia. The electrolytes in the cathode and acid trap were both collected and analyzed for quantitative measurements.

Detection of hydrazine by Watt and Chrisp method. The indicator solution for hydrazine was prepared by dissolving 0.6 g of para-(dimethylamino) benzaldehyde in 30 mL absolute ethanol and 3 mL concentrated HCl (35%). 2 mL of this color agent was mixed with the same volume of the electrolyte solution and the mixture was then incubated in dark for 15 minutes before performing the UV-vis characterization.[1] A set of solutions with the known concentration of N_2H_4 in 0.1 M Na_2SO_4 was used as a calibration standard and their absorbance was measured at λ = 460 nm.

^{1}H NMR studies. NMR measurements were carried out with DMSO-d^6 as solvent. Prior to NMR sample preparation, the electrolyte solution was concentrated to 1 mL and a quantitative amount of the sample was added to DMSO-d^6 and subjected to 6000 scans for getting a proper triplet signal (with coupling constant *j*=52 Hz) for $^{14}NH_4^+$ and doublet for $^{15}NH_4^+$ (coupling constant *j*=72 Hz). It is to be noted that, the coupling constant values are calculated as a product of the chemical shift value (δ in ppm) and 400 MHz (spectrometer frequency) using equation 2.

$$\delta(ppm) = j(Hz)/spectrometer\ frequency\ (MHz) \quad (2)$$

Quantification of NH_3 Concentration from NMR. The catholyte solution was concentrated to 1 mL and 400 µL was taken out of it for NMR analysis. This was subsequently added with 50 µL of 0.01 M maleic acid solution followed by DMSO-d^6 and subjected to ^{1}H-NMR study. The obtained peaks were integrated and by using the following equation 3, the concentration of NH_3 was quantified and matched with that obtained from UV–visible spectroscopic method.

$$(I_{sample})/(I_{standard}) = (H_{sample} \times C_{sample})/(H_{standard} \times C_{standard}) \quad (3)$$

where *I* stands for the integral values, H stands for the number of protons (4 in case of sample NH_4^+ and 2 in case of the vinylic protons of maleic acid) and *C* stands for the concentrations of the sample and standard (0.01 M for maleic acid).

$^{15}N_2$- isotope Labeling Experiments. $^{15}N_2$ (Sigma Aldrich, 98 atom% $^{15}N_2$) was used as the feeding gas in the labelling experiment. Before feeding the electrolyte solution with $^{15}N_2$, the electrolyte was degassed using Ar for an hour. A low-velocity gas flow system was adopted due to the limited supply and expense of $^{15}N_2$. After electrolysis at -0.3 V vs. RHE for 1 h, the electrolyte was further added to 37%-concentrated HCl and concentrated using Buchi Rotavapor, followed by addition of 0.01 M maleic acid and 0.4 ml of D^6-DMSO. The produced ammonia was quantified using ^{1}H nuclear magnetic resonance measurements in a 400 MHz Bruker Advance II 400 NMR spectrometer.

In-situ FTIR studies. In-situ FTIR studies were carried out with Si face angle crystal in a spectro-electrochemical cell equipped with a three-electrode set-up. The background was collected with the electrolyte and all the sample measurements were taken with 128 scans and resolution 4 in absorbance mode. All data were further baseline corrected and were collected by holding different cathodic potentials for a definite time-span.

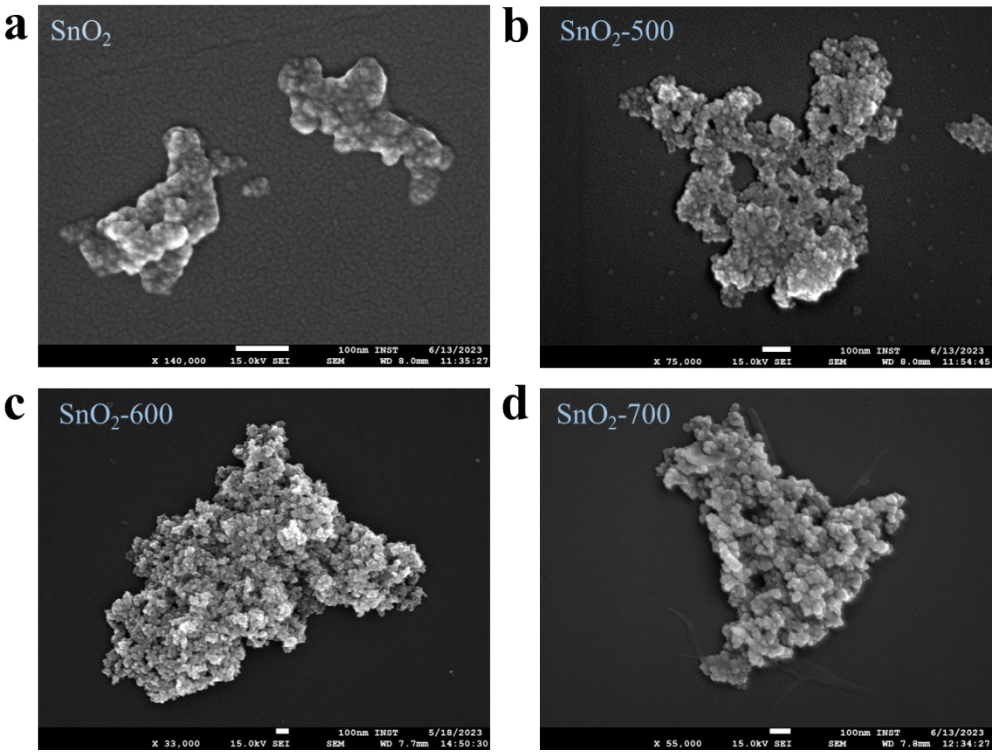

Fig. S1. FESEM images of (a) SnO_2, (b) SnO_2-500, (c) SnO_2-600 and (d) SnO_2-700 samples, (scale bar: 100 nm).

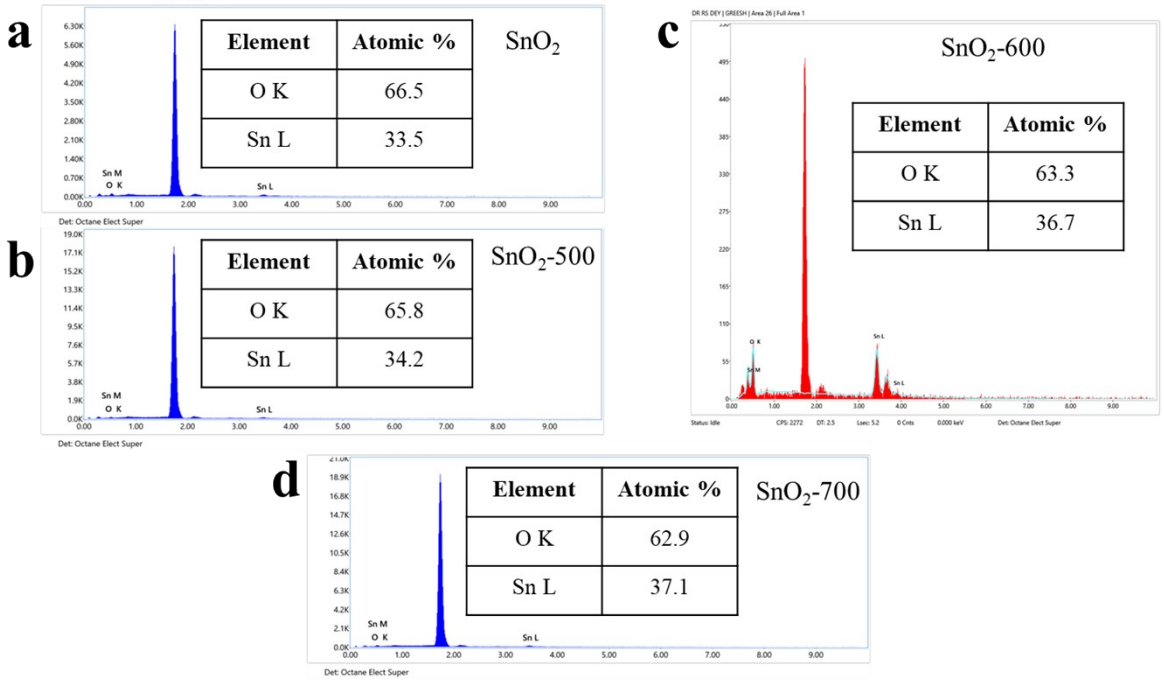

Fig. S2. EDS elemental analyses of (a) SnO_2, (b) SnO_2-500, (c) SnO_2-600 and (d) SnO_2-700 samples; inset shows the atomic % of Sn and O in all the samples respectively.

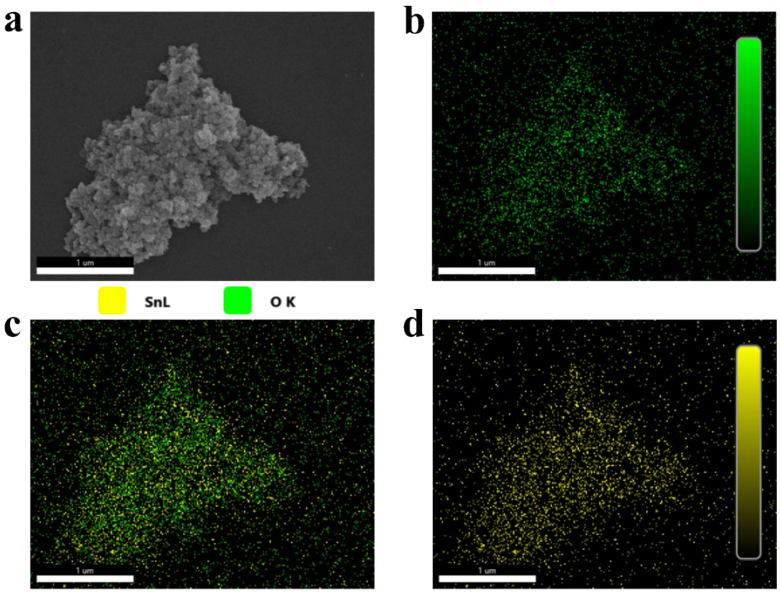

Fig. S3. (a-d) EDS mapping of SnO_2-600 catalyst showing the presence of Sn and O elements in the sample.

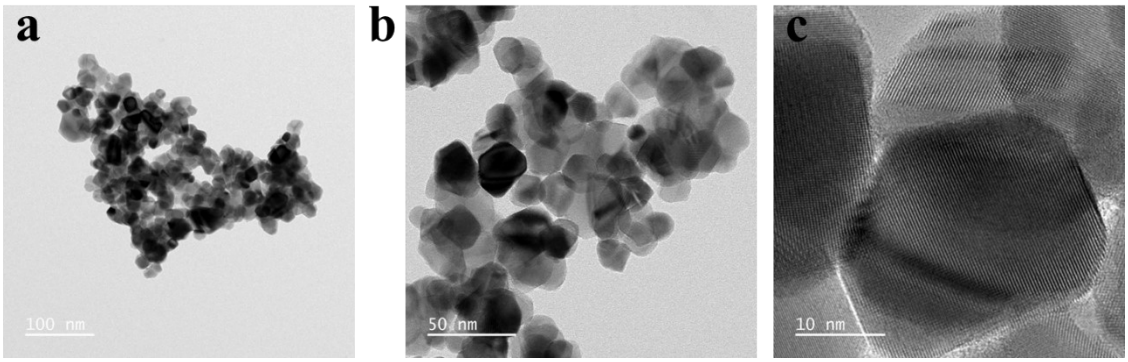

Fig. S4. (a-c) TEM images of SnO_2-600 catalyst at different optical resolutions (100 nm, 50 nm and 10 nm respectively).

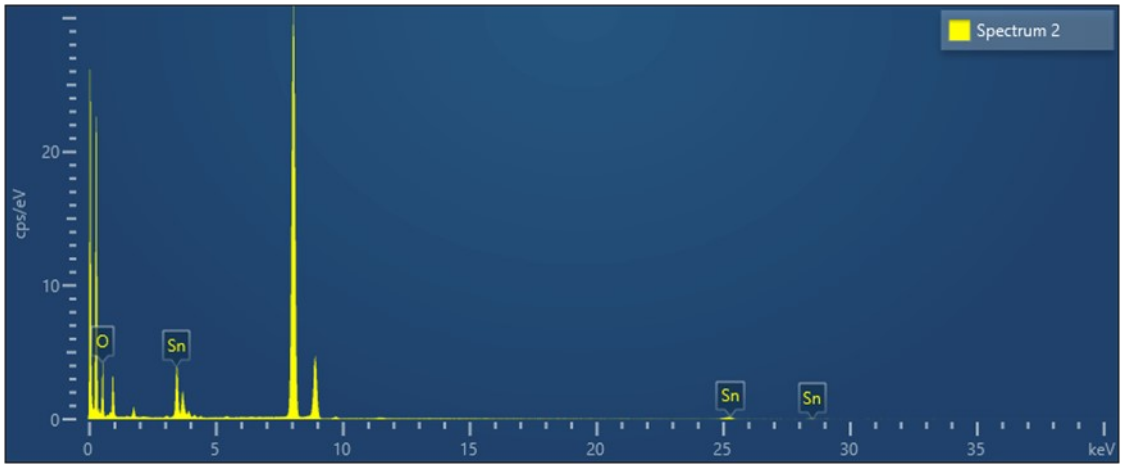

Fig. S5. EDS Spectrum of SnO_2-600 showing the presence of Sn and O as constituting elements.

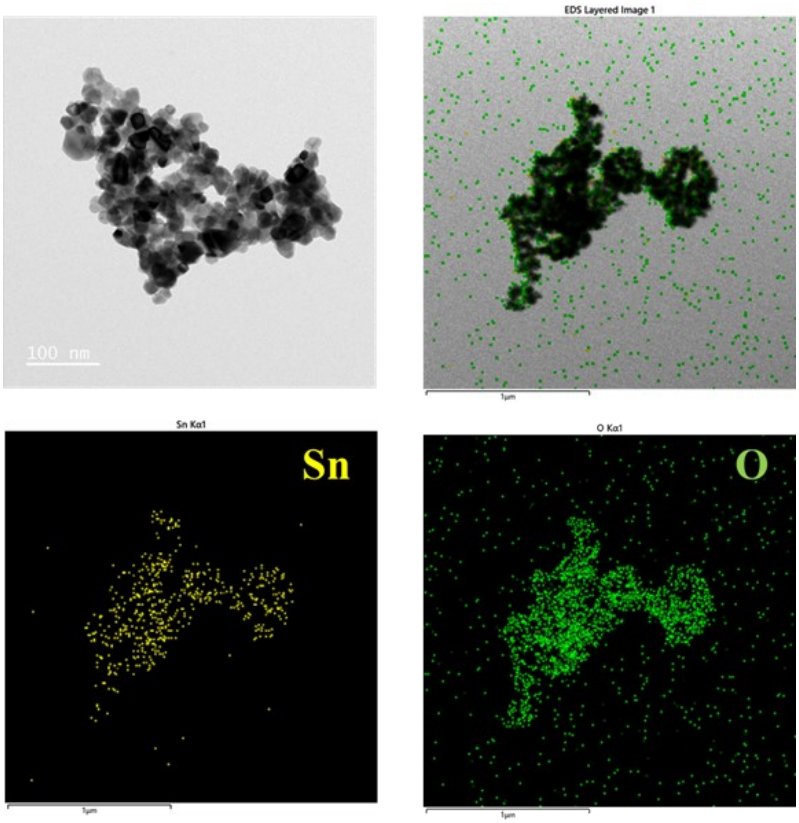

Fig. S6. TEM image of SnO2=600 sample and corresponding cumulative and individual elemental mapping of the sample representing Sn and O atoms (scale bar-100 nm).

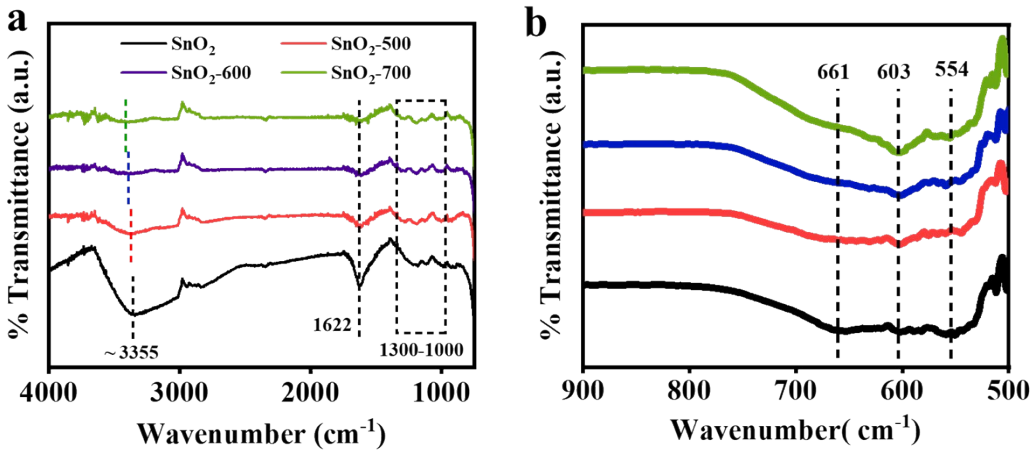

Fig. S7. (a) and (b) represent the FTIR spectra of all SnO_2 samples denoting different peaks for the different Sn-O type stretches.

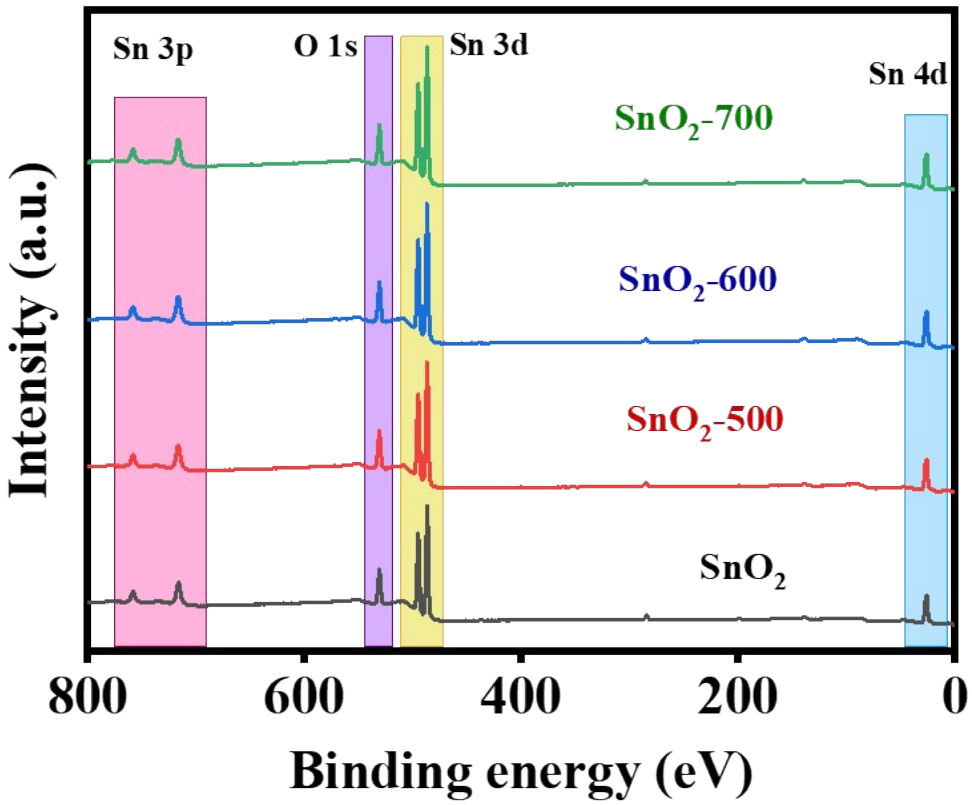

Fig. S8. XPS full survey spectra of all SnO_2 samples, the colored boxes in the inset resemble peaks for O 1s, Sn 3d, Sn3p as well as Sn 4d.

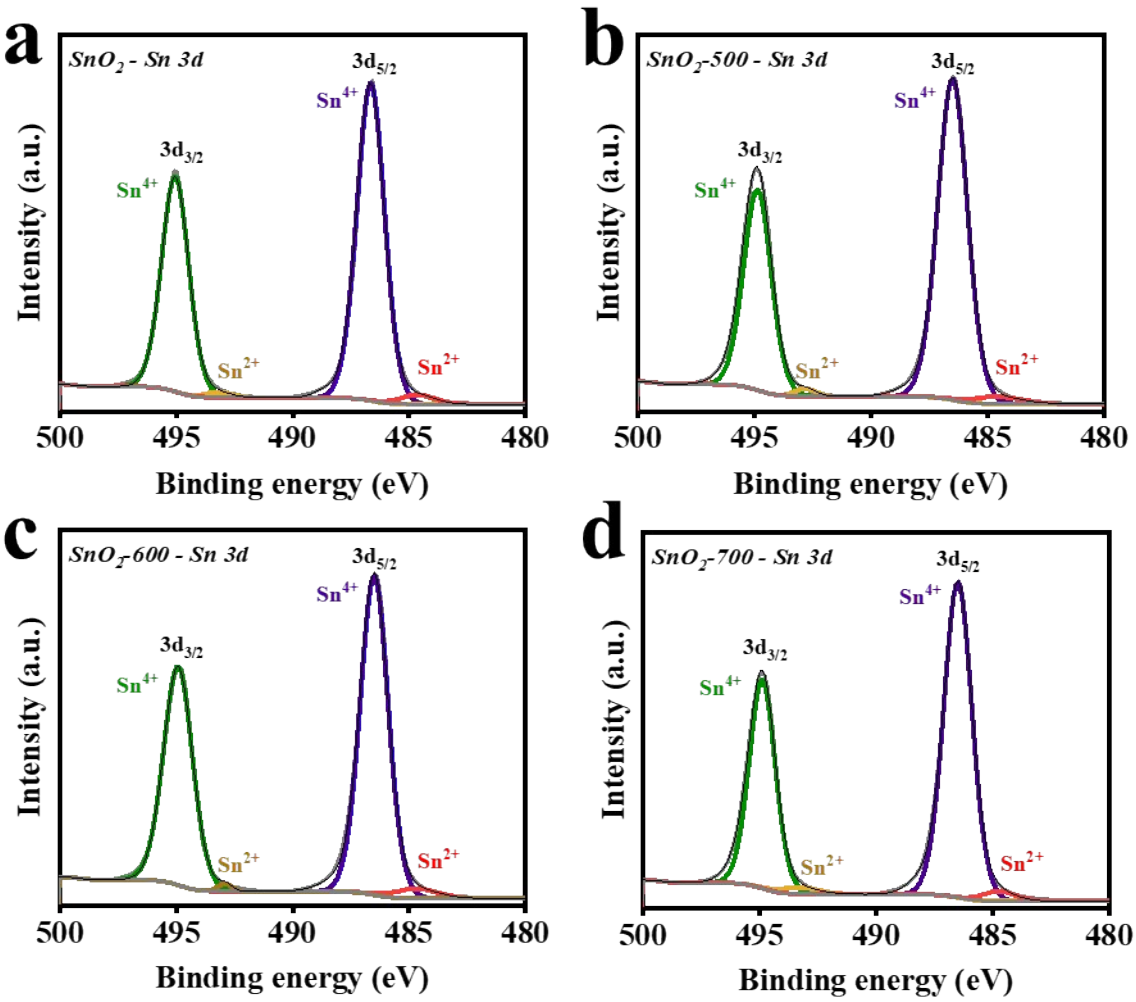

Fig. S9. XPS deconvoluted narrow spectra of Sn 3d for (c) SnO_2, (d) SnO_2-500, (e) SnO_2-600, (f) SnO_2-700.

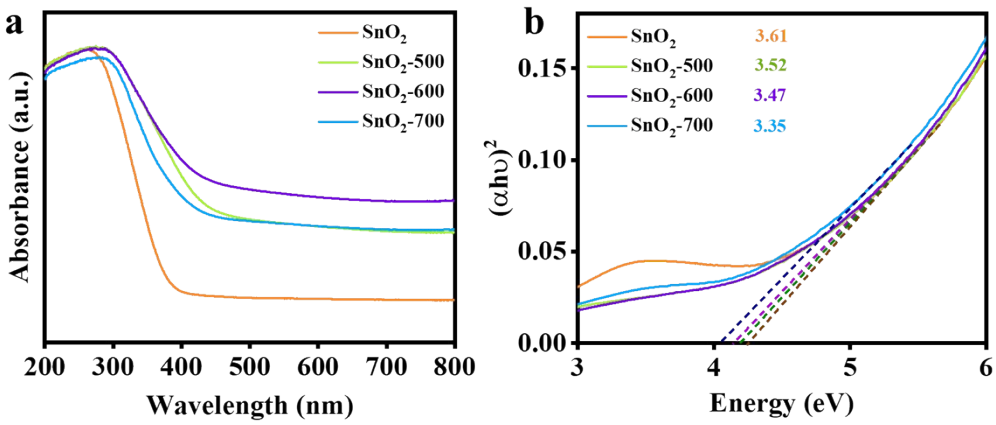

Fig. S10. (a) Diffused reflectance UV-visible spectra of all the catalysts; (b) corresponding Tauc plot for deriving band gap values obtained by extrapolating the tangents cutting the x-axis.

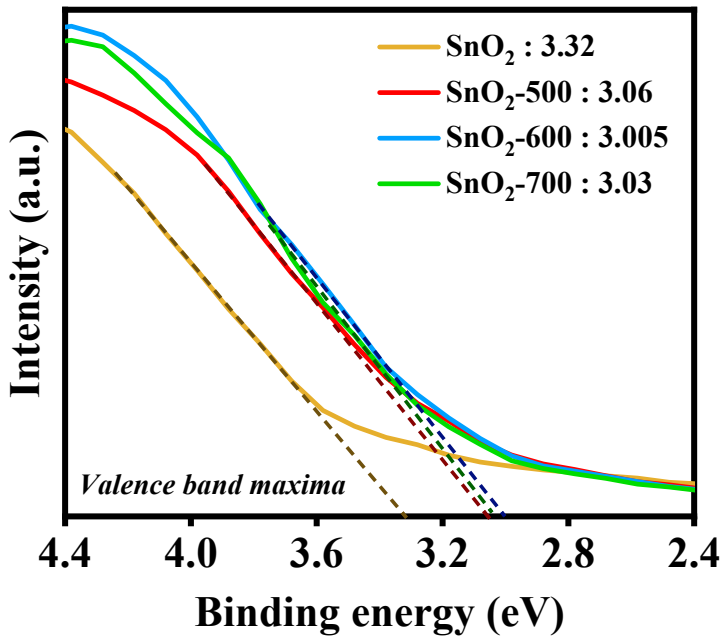

Fig. S11. Surface valence X-ray photoelectron spectra of all samples representing the valence band maxima at the cut point on x-axis obtained by extrapolating the tangents for each of the plots.

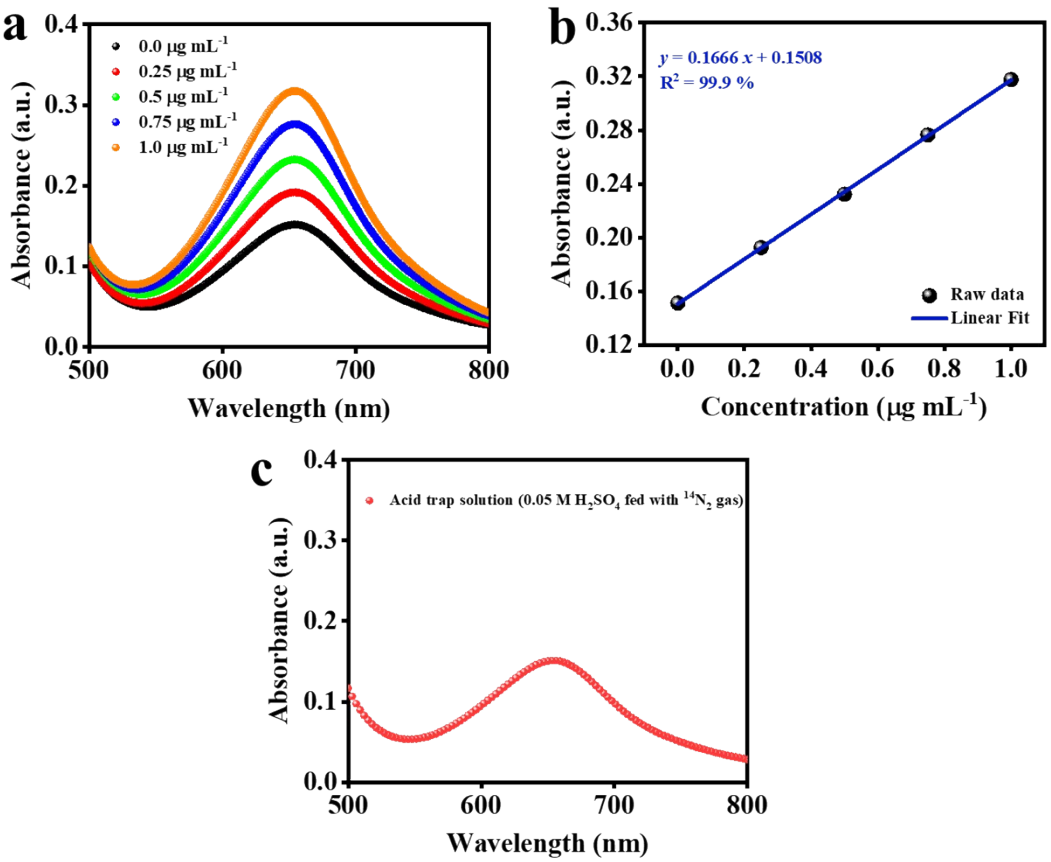

Fig. S12. (a) UV-vis spectra of 0.05 M H_2SO_4 containing different known concentrations of NH_4^+ stained with indophenol blue indicator solutions after 2 h incubation at room temperature and (b) corresponding absorbance calibration plot used to quantify the impurity content in acid trap; (c) Indophenol blue method of spectrophotometric analysis of ammonia in 0.05 M H_2SO_4 trap solution.

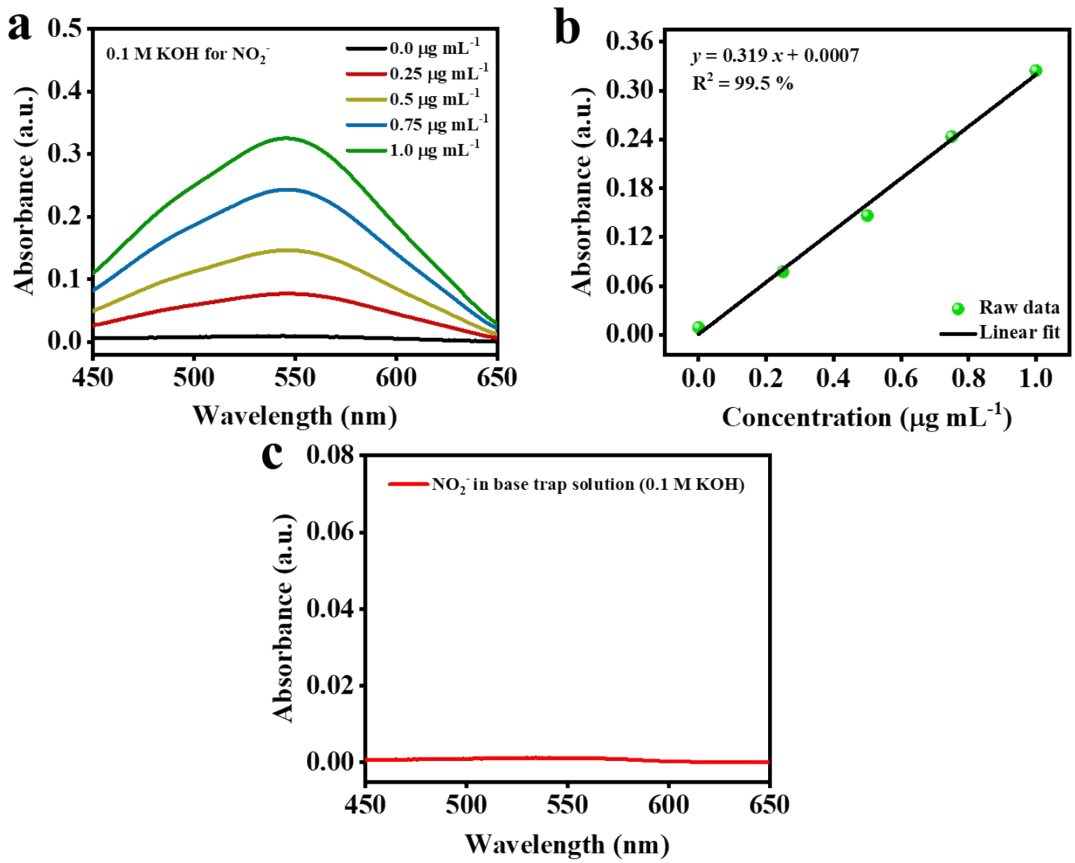

Fig. S13. (a) Calibration for the spectrophotometric analysis of known concentration of NO_x in 0.1 M KOH base trap solution following Griess method; (b) shows corresponding linearly fitted calibration plots; (c) Spectroscopic analysis for the detection of NO_x dissolved in the 0.1 M KOH trap solution from $^{14}N_2$ gas.

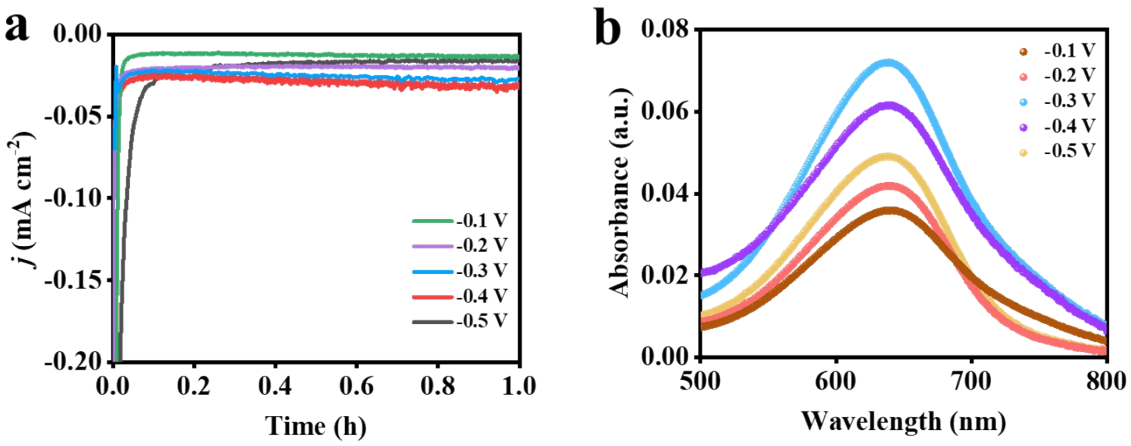

Fig. S14. (a) Potential dependent chronoamperometric curves of SnO_2-600 catalyst for 1 h run (each) in 0.1 M Na_2SO_4 electrolyte, (b) UV-vis absorption spectra of the electrolyte (0.1 M Na_2SO_4 with dissolved NH_4^+) stained with indophenol blue indicator at different potentials after 2 h of incubation from the chronoamperometric run for SnO_2-600 catalyst.

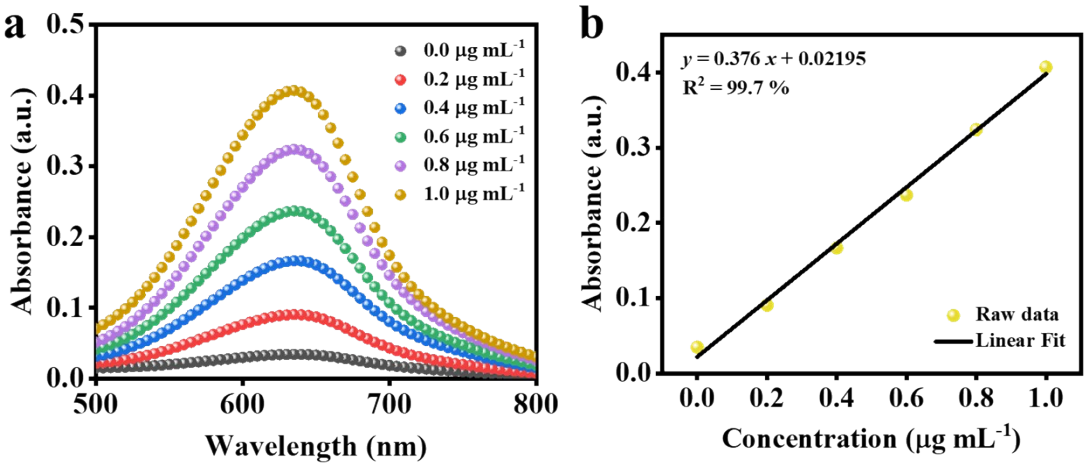

Fig. S15. (a) UV-vis spectra of 0.1 M electrolyte solutions, demonstrating different known concentrations of NH_4^+ stained with indophenol blue indicator solutions after 2 h incubation at room temperature and (b) corresponding absorbance calibration plot used in this study.

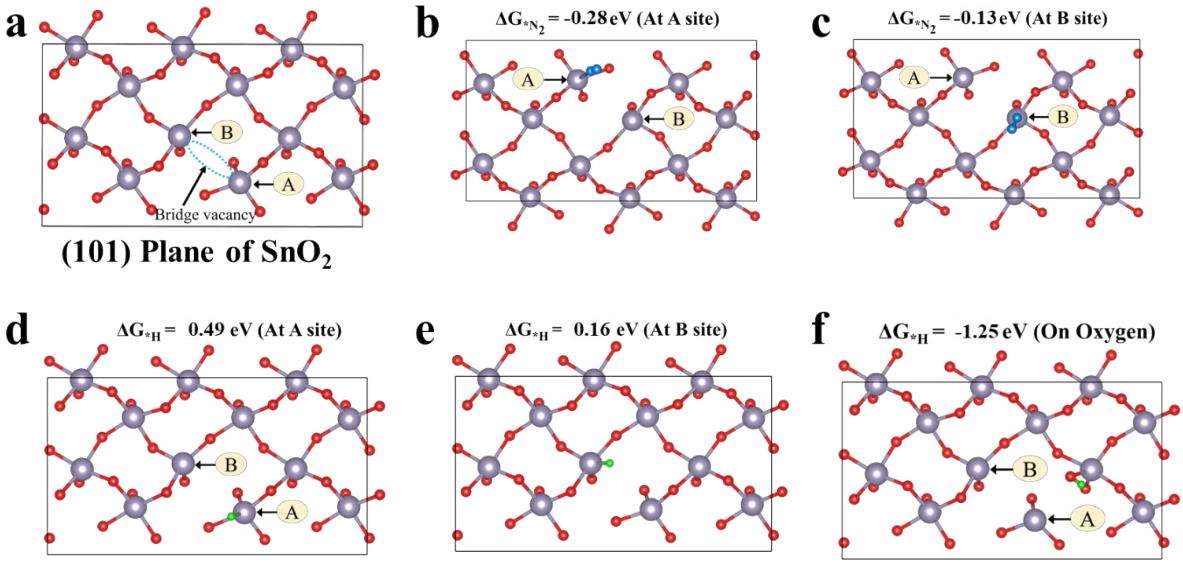

Fig. S16. (a) shows the optimized structure of (101) planes of SnO_2 with bridge oxygen vacancy (bo_v), (b) and (c) represent the optimized structures of adsorption of N_2 on different Sn atoms named as A and B sites respectively, (d), (e) and (f) represent the optimized structures of adsorptions of H atom on three possible active sites- two Sn atoms called as A and B near oxygen vacancy and an oxygen atom respectively. Grey, red, blue and green colours represent Sn, O, N and H atoms respectively.

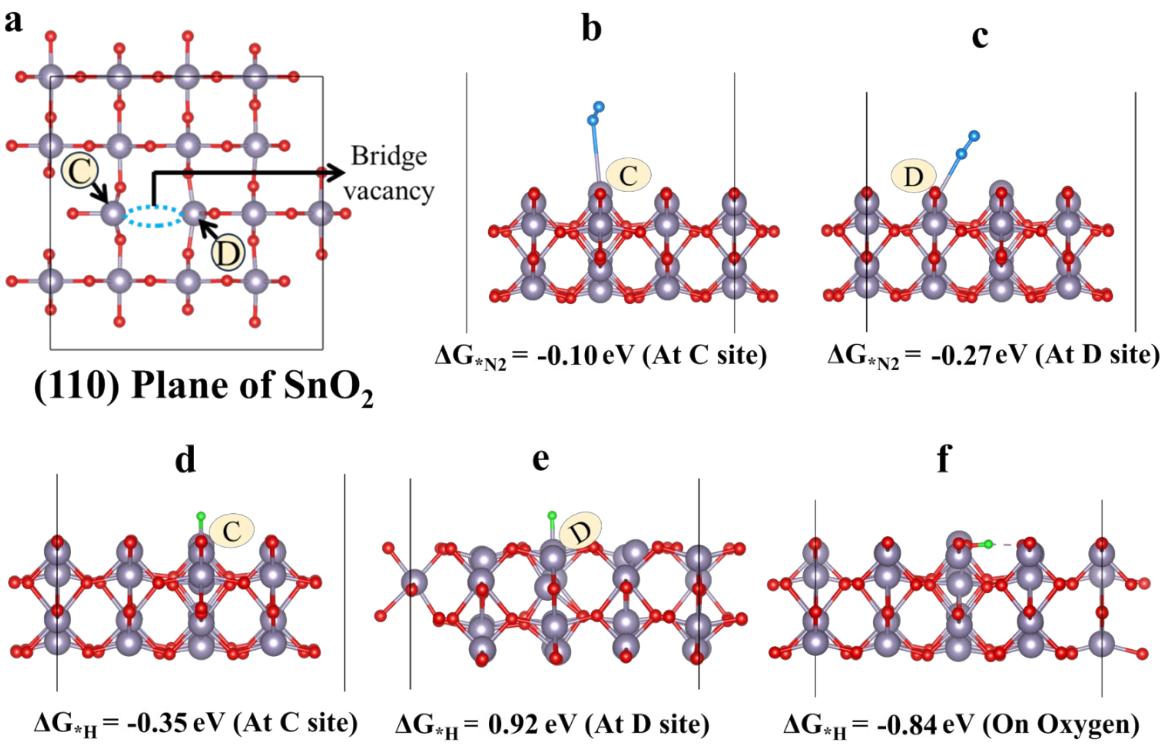

Fig. S17. (a) shows the top view of optimized structure of (110) oriented SnO_2 film, (b) and (c) represent the optimized structures of N_2 adsorptions at two different Sn atoms called as C and D sites, (d), (e) and (f) represent the optimized structures of H adsorptions on three different active sites- two Sn atoms called as C and D and an oxygen atom respectively. Grey, red, blue and green colours represent Sn, O, N and H atoms respectively.

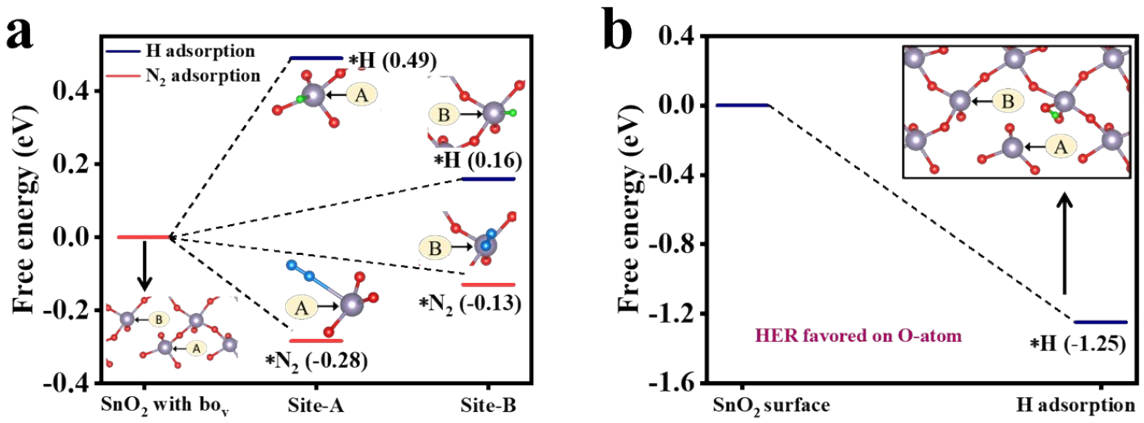

Fig. S18. (a) Comparison of free energies between N_2 and H adsorptions on Sn (A site) and Sn (B site) respectively of SnO_2 (101) with bo_v, (b) Free energy for H adsorption on O-atom site of SnO_2 (101) with bo_v.

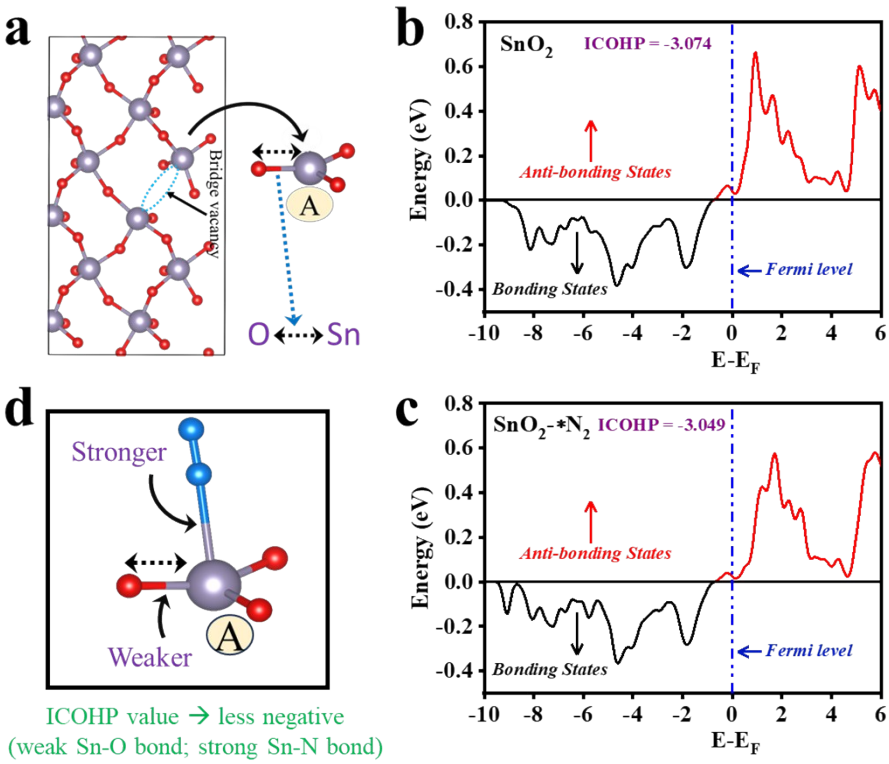

Fig. S19. (a) Schematic representation of SnO_2 (101) plane with bov showing Sn-O bond for which crystal orbital Hamiltonian populations (COHP) calculation was carried out, (b) ICOHP of SnO_2 and (c) N_2 adsorbed SnO_2 and (d) the corresponding representation of Sn (site-A)-O bond strength with respect to Sn-N binding.

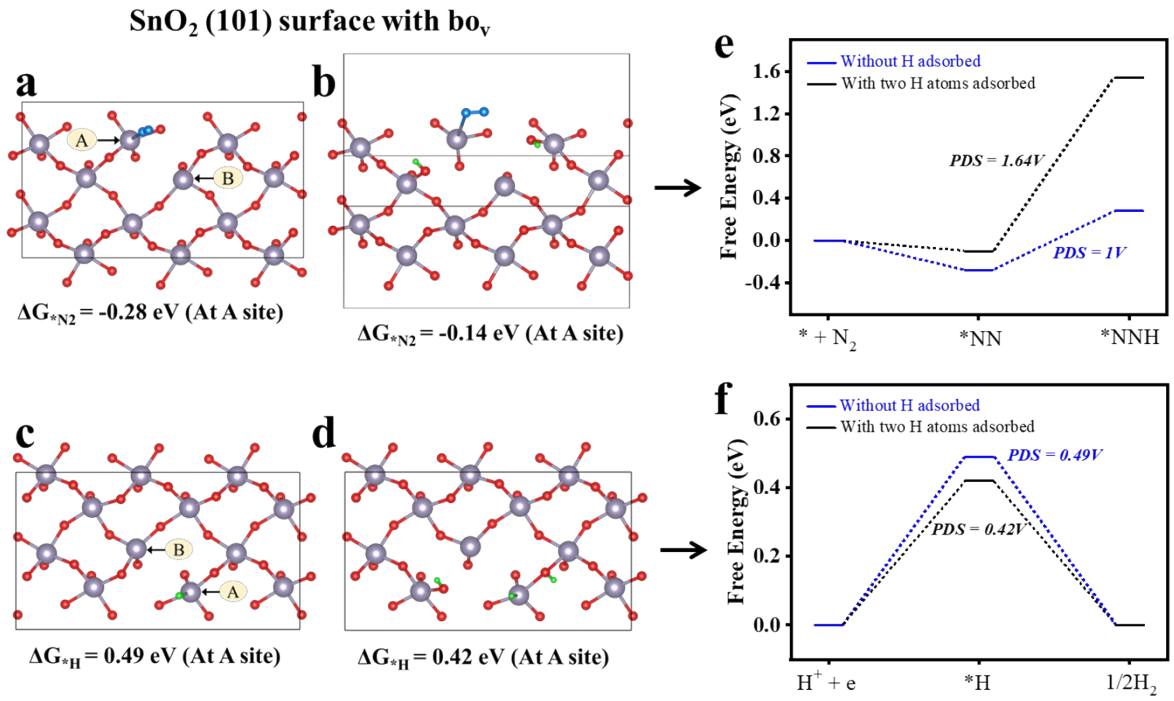

Fig. S20. Model structure of SnO_2 (101) plane with bo_v with free energy values of N_2 adsorbed on site-A Sn atom with (a) and without (b) pre-adsorbed protons, model structure with free energy values of H adsorbed on site-A Sn atom with (c) and without (d) pre-adsorbed protons, corresponding free energy plots in case of (e) N_2 adsorption and (f) H adsorption.

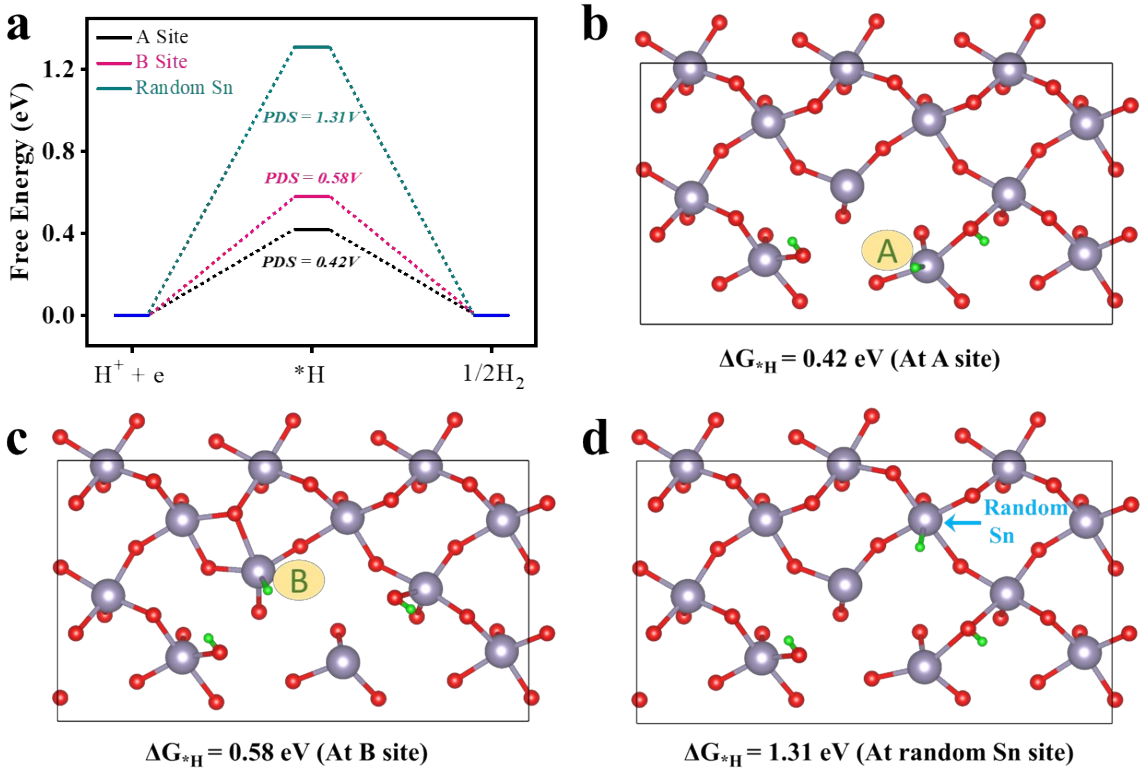

Fig. S21. (a) Free energy for H adsorption of Site-A/B and random Sn site in a proton pre-adsorbed bo_v dominated (101) lattice, Model structure of SnO_2 (101) plane with bo_v with H adsorbed on (b) site-A Sn atom, (c) site-B Sn atom and (d) random Sn atom, besides two pre-adsorbed protons on more electronegative O-atoms.

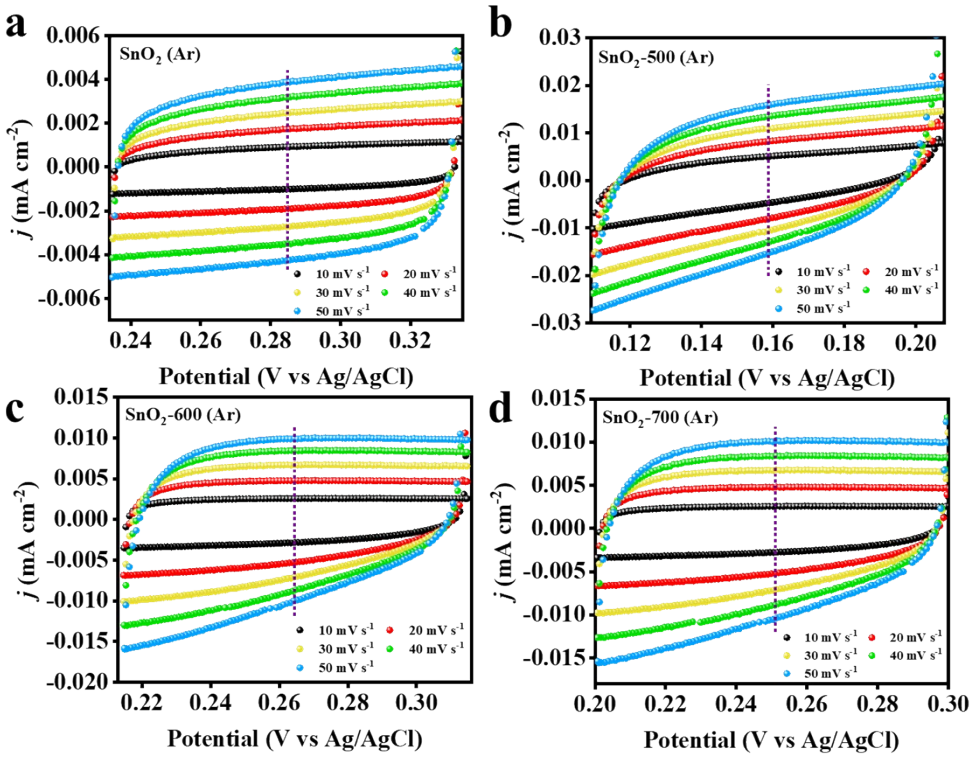

Fig. S22. CV analysis in the non-Faradaic potential region at scan rate 10-50 mV s^{-1} for (a) SnO_2, (b) SnO_2-500, (c) SnO_2-600 and (d) SnO_2-700 catalysts under Ar.

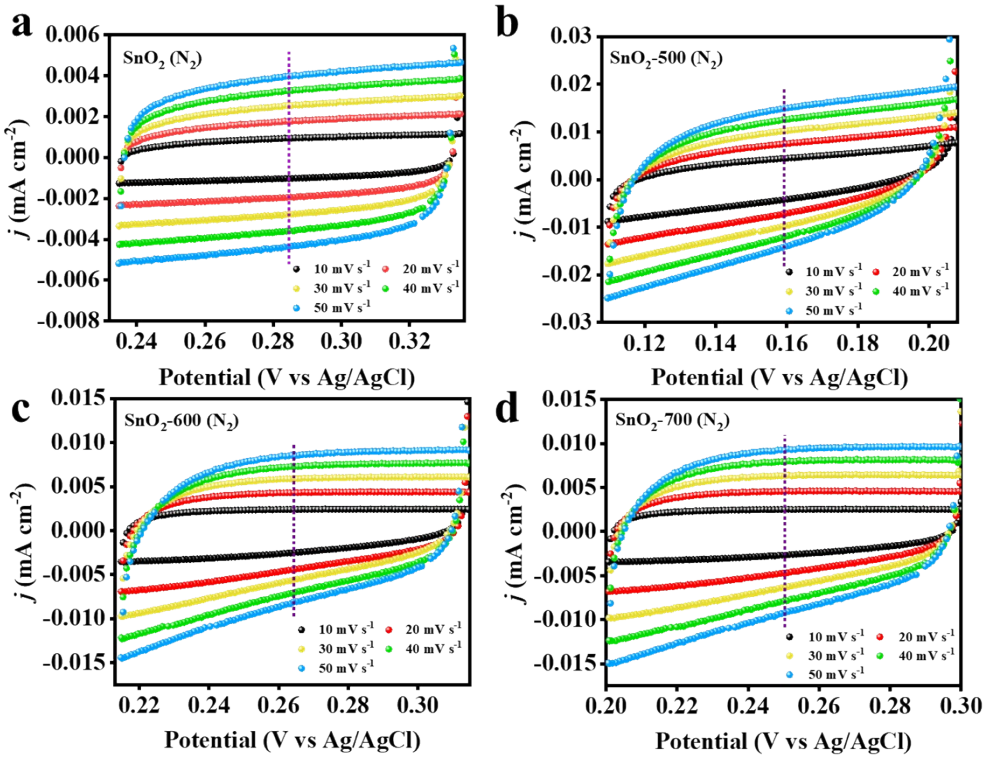

Fig. S23. CV analysis in the non-Faradaic potential region at scan rate 10-50 mV s^{-1} for (a) SnO_2, (b) SnO_2-500, (c) SnO_2-600 and (d) SnO_2-700 catalysts under N_2.

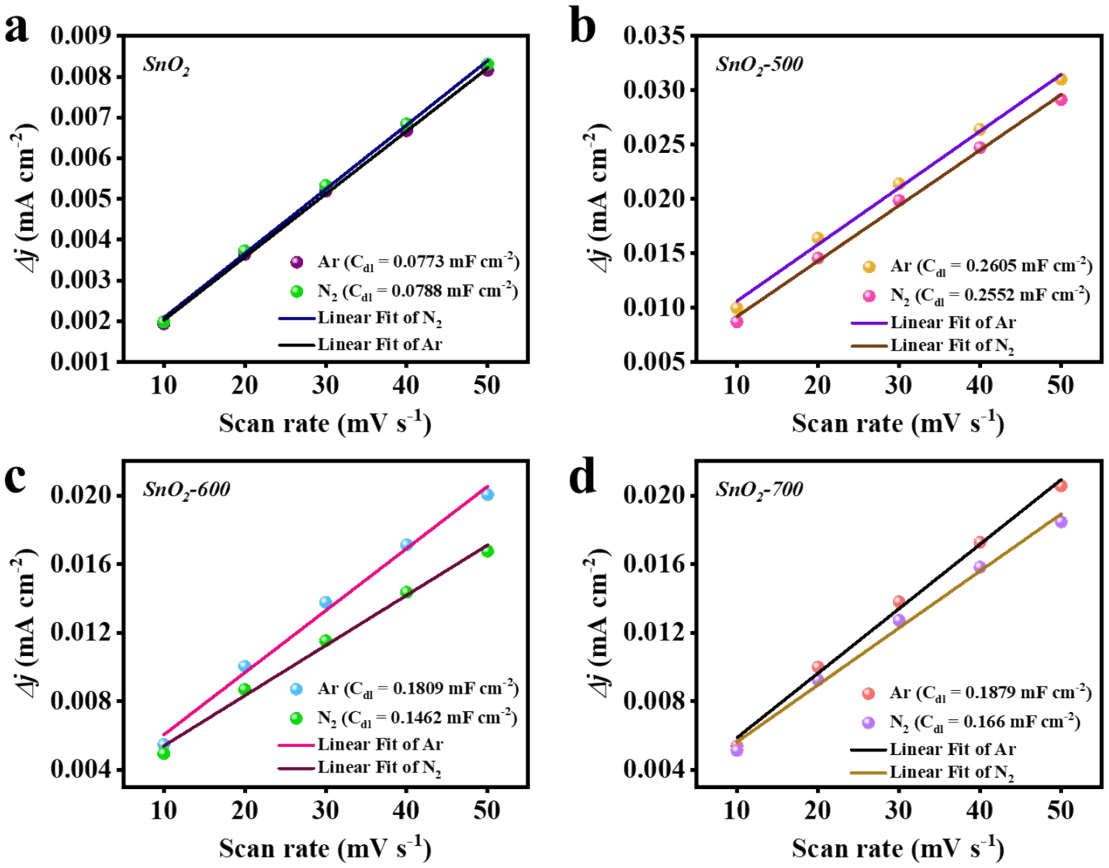

Fig. S24. Comparative linear regression plot and the derived double layer capacitance (C_{dl}) of all SnO_2 catalysts under Ar and N_2, respectively.

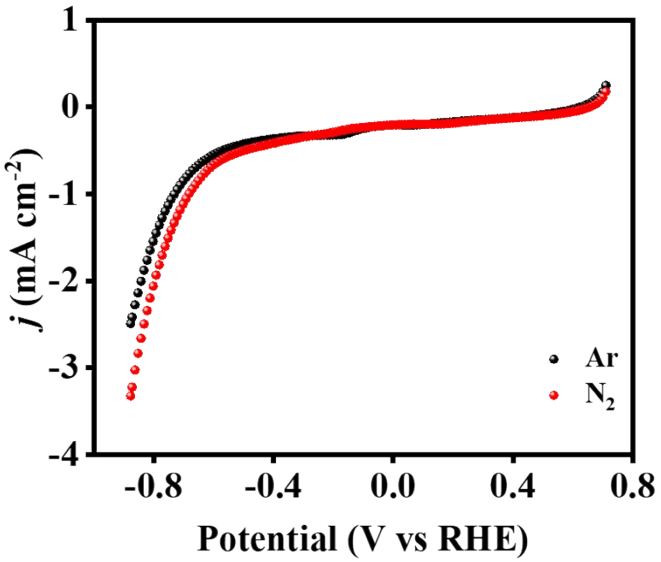

Fig. S25. Comparative LSV curve for SnO_2-600 catalyst at 10 mV s^{-1} scan rate in N_2 and Ar purged 0.1 M Na_2SO_4.

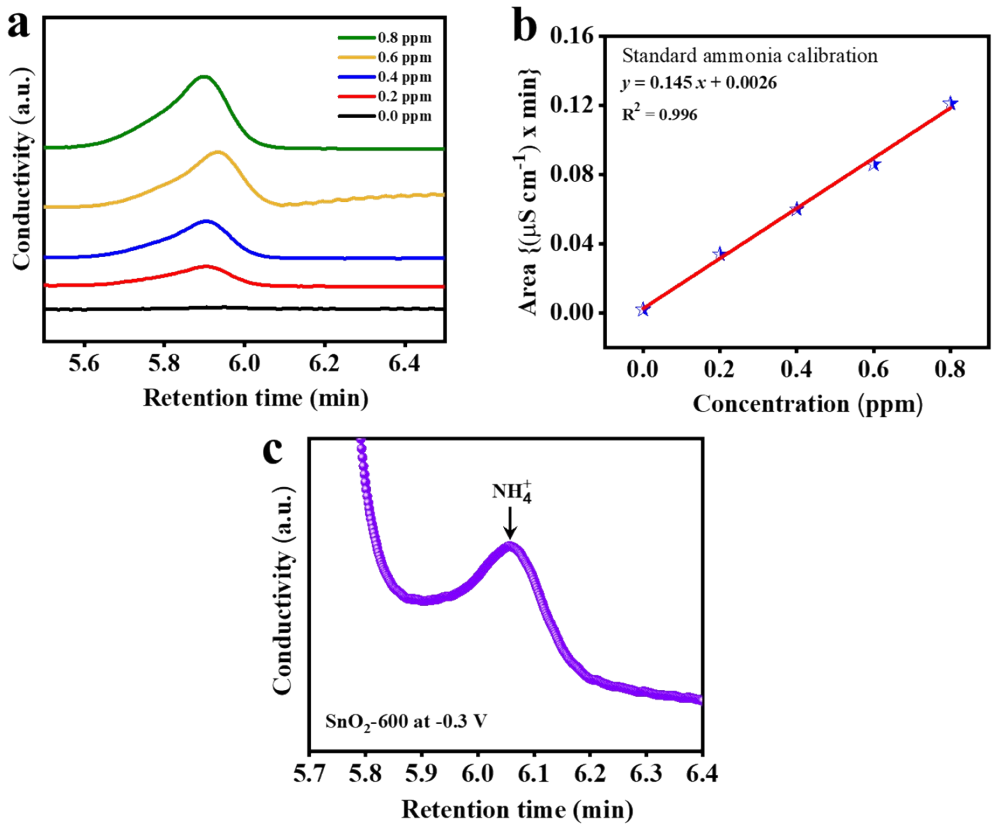

Fig. S26. (a) Calibration plot for the different standard concentrations of ammonium ion, derived from ion chromatography measurements, (b) corresponding linear fitting of the data points (inset shows the derived calibrated equation used in this study, (c) ion chromatography data of the electrolyte solution containing NH_4^+ formed during the chronoamperometric run at -0.3 V in neutral electrolyte with SnO_2-600 catalyst in presence of N_2.

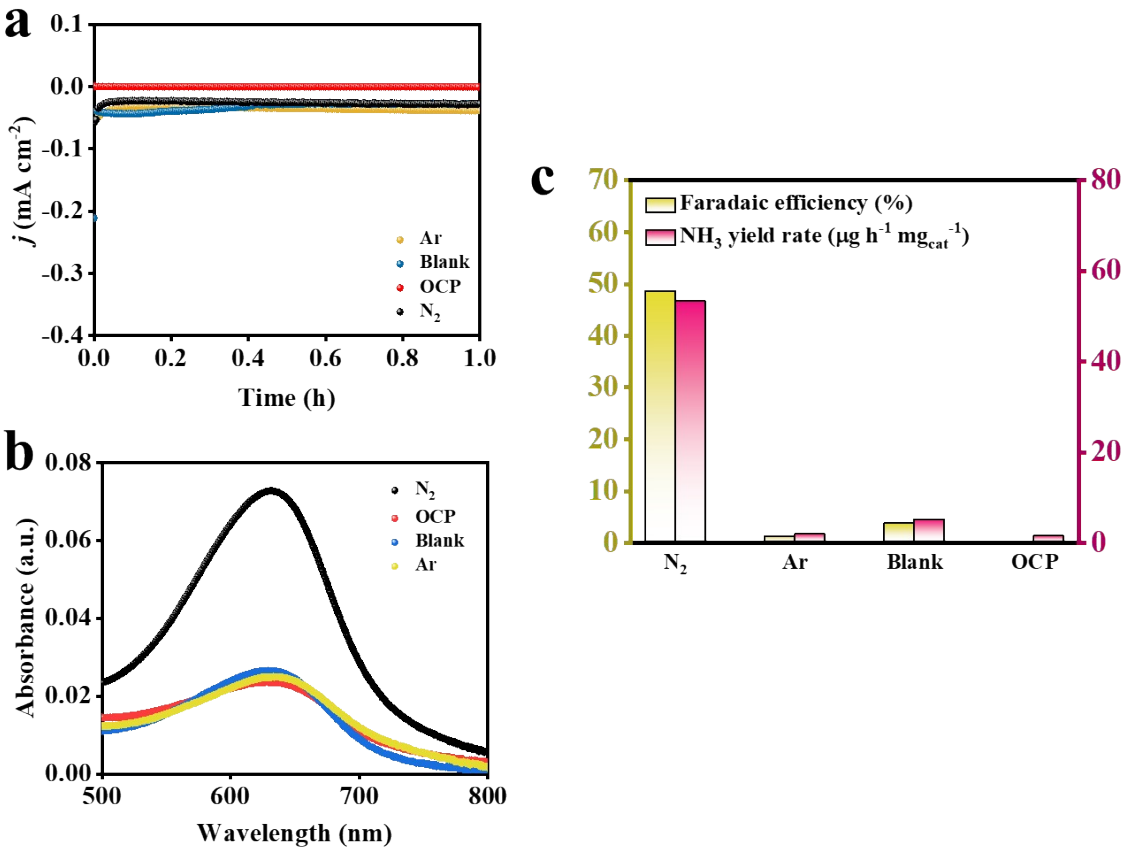

Fig. S27. (a) Chronoamperometric curves of SnO_2-600 catalyst for 1 h run (each) in 0.1 M Na_2SO_4 electrolyte under N_2 (at -0.3 V as well as open circuit potential), Ar (at -0.3 V) and for blank substrate in N_2 at -0.3 V vs. RHE, (b) corresponding UV-vis absorption spectra of the electrolyte (0.1 M Na_2SO_4 with dissolved NH_4^+) stained with indophenol blue indicator at different potentials after 2 h of incubation from the chronoamperometric run, plot also includes OCP data and (c) comparative Faradaic efficiency and yield rate under all conditions.

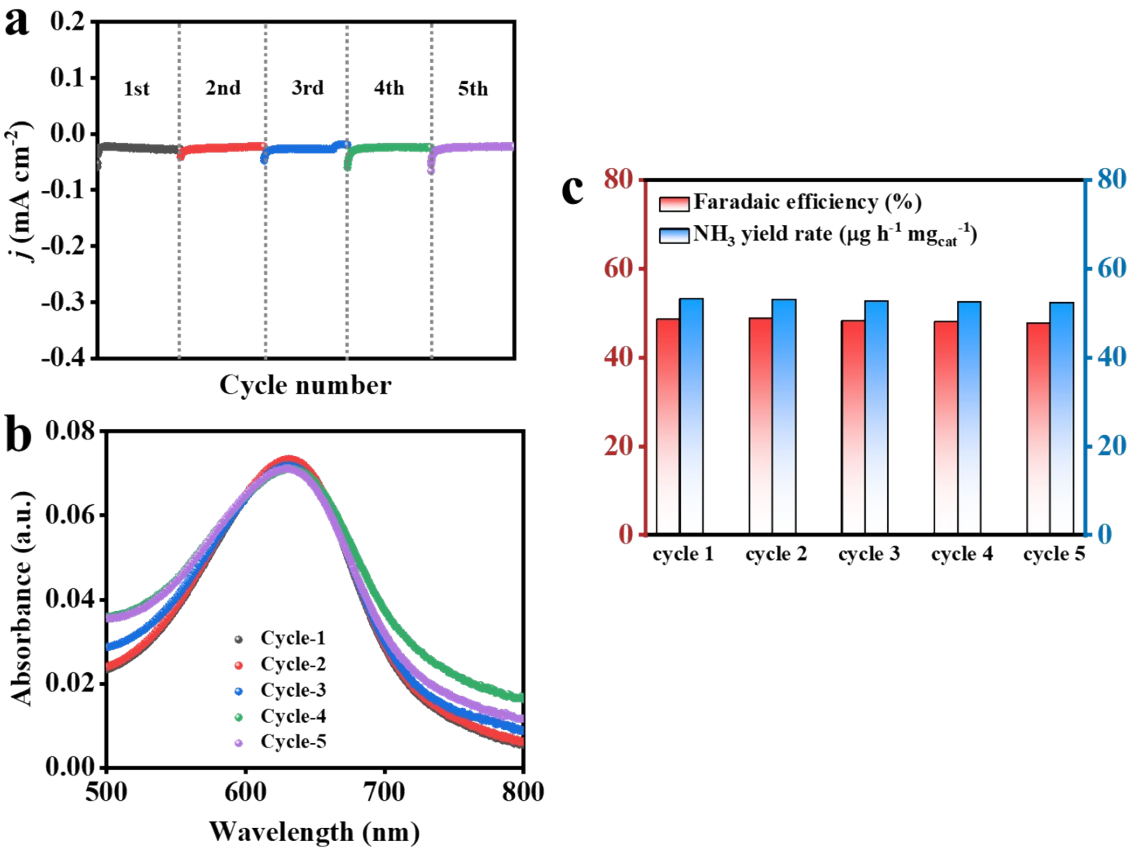

Fig. S28. (a) Chronoamperometric curves of SnO_2-600 catalyst in N_2 saturated 0.1 M Na_2SO_4 at -0.3 V vs RHE for five consecutive cycles (each for 1 h). (b) UV-vis absorption spectra of the electrolyte for detection of the evolved NH_3 for five consecutive chronoamperometric cycles (each for 1 h) at -0.3 V vs RHE. (c) Yield rate of NH_3 and F.E. after cycling experiments.

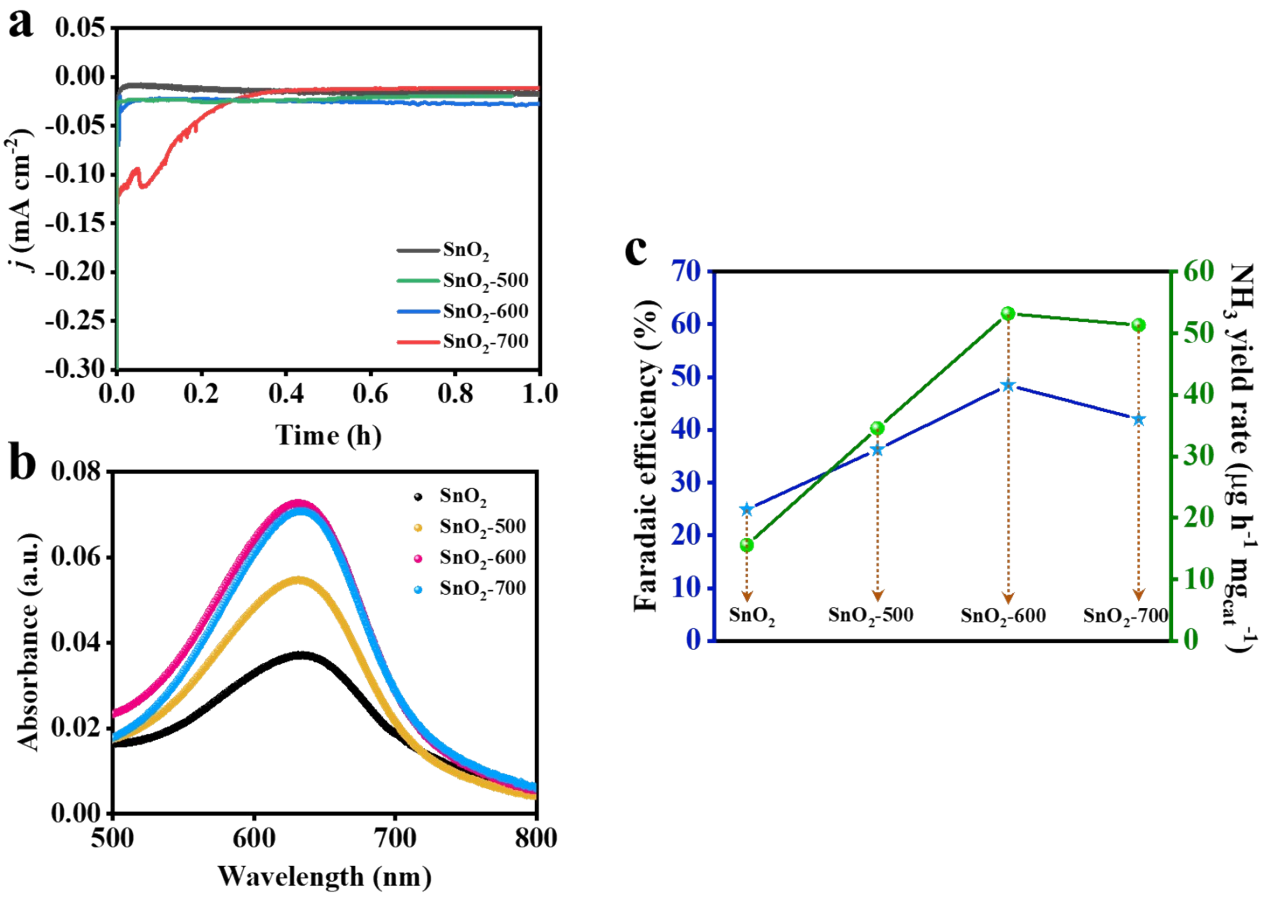

Fig. S29. (a) Chronoamperometric curves of different SnO_2 catalysts for 1 h run (each) in 0.1 M Na_2SO_4 electrolyte at -0.3 V, (b) UV-vis absorption spectra of the electrolyte (0.1 M Na_2SO_4 with dissolved NH_4^+) stained with indophenol blue indicator for the different dopant loaded catalysts at -0.3 V after 2 h of incubation from the chronoamperometric run, and (c) comparative yield rate and faradaic efficiency of all catalysts.

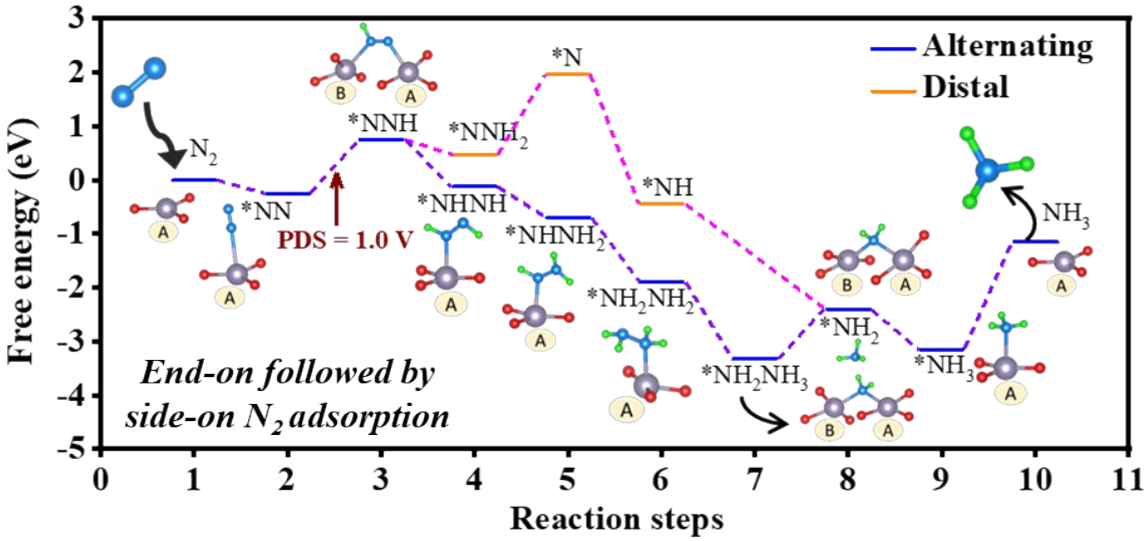

Fig. S30. Full free energy profile of NRR showing possibilities of alternating and distal mechanistic pathways for N_2 reduction on SnO_2.

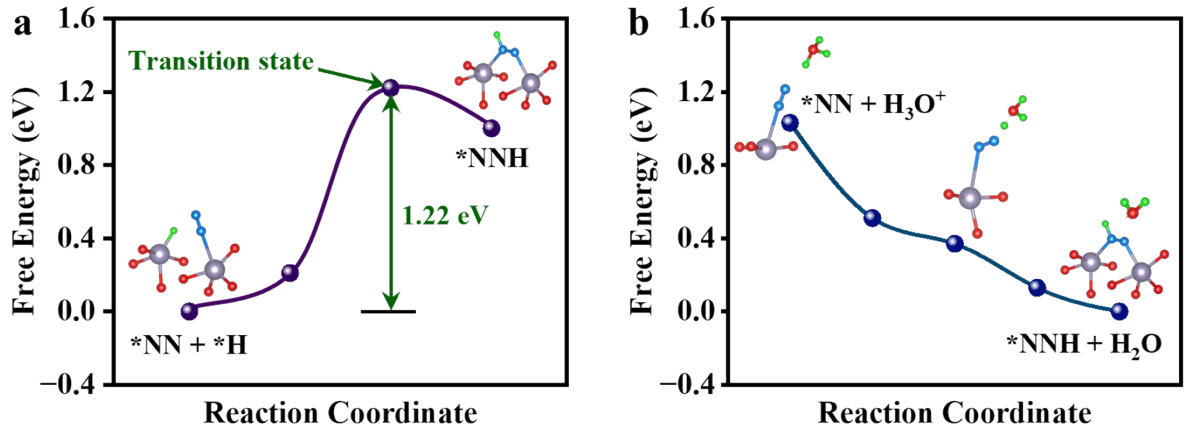

Fig. S31. (a) Plot of free energy change vs. first protonation step with optimized initial and final states, showing the transition state; (b) Plot of free energy change vs. first protonation step with optimized initial, one middle and final states. Blue, red, green colours atoms stand for nitrogen, oxygen and hydrogen atom respectively and big atom is Sn.

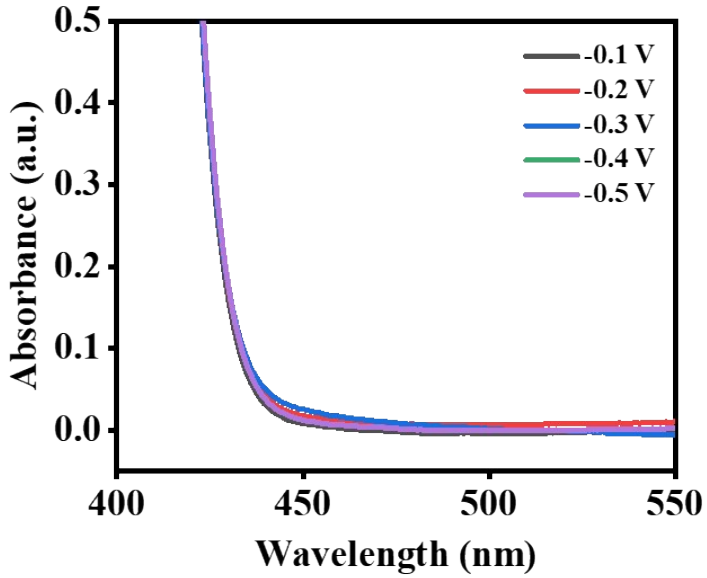

Fig. S32. UV-vis absorption spectra for the detection of N_2H_4 at different applied potentials for 1 h of NRR measurements for SnO_2-600 catalyst in 0.1 M Na_2SO_4.

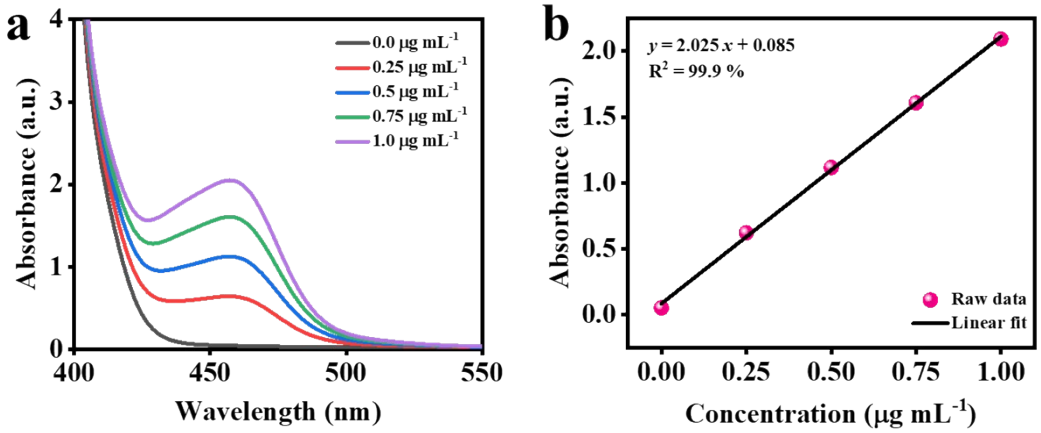

Fig. S33. (a) UV-vis spectra representing different known concentrations of N_2H_4 at 460 nm after 15 min incubation at room temperature. (b) corresponding absorbance calibration plot used in this study.

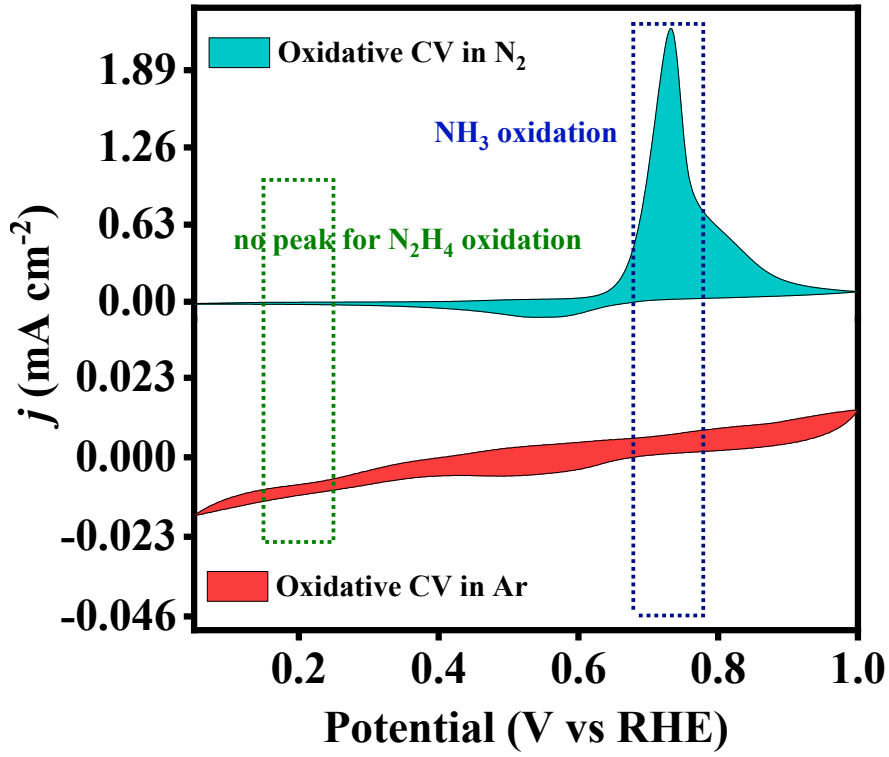

Fig. S34. Cyclic voltammetry scans on Pt ring taken in the oxidative region at 10 mV s^{-1} in Ar and after NRR experiments in N_2; GC part of RRDE covered with SnO_2-600 catalyst.

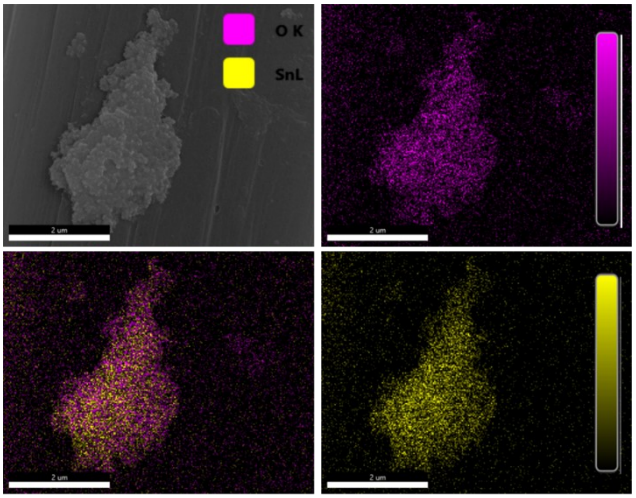

Fig. S35. FESEM image and elemental mapping of SnO_2-600 catalyst after electrocatalytic NRR stability test.

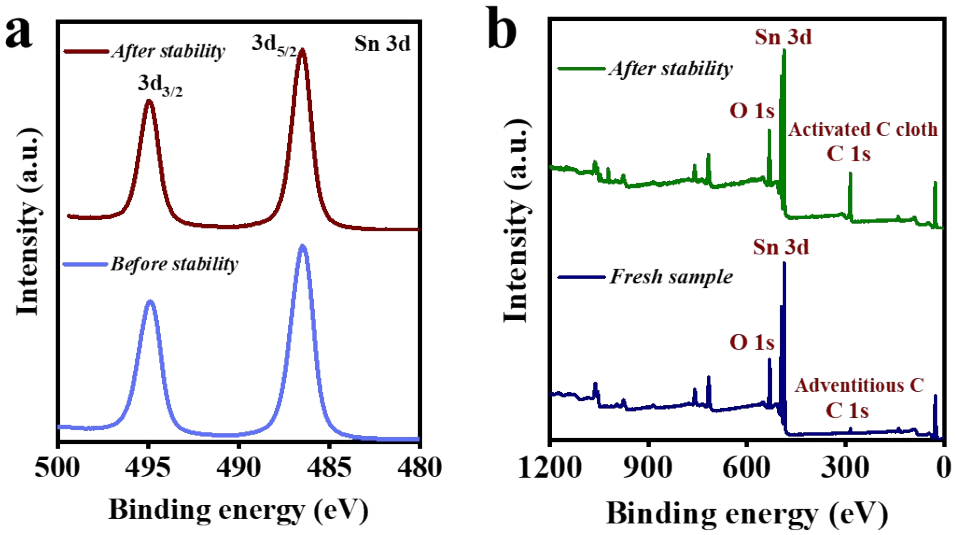

Fig. S36. Comparative (a) XPS narrow spectra of Sn 3d and (b) full survey spectra of SnO_2-600 catalyst after 24 h of stability study.

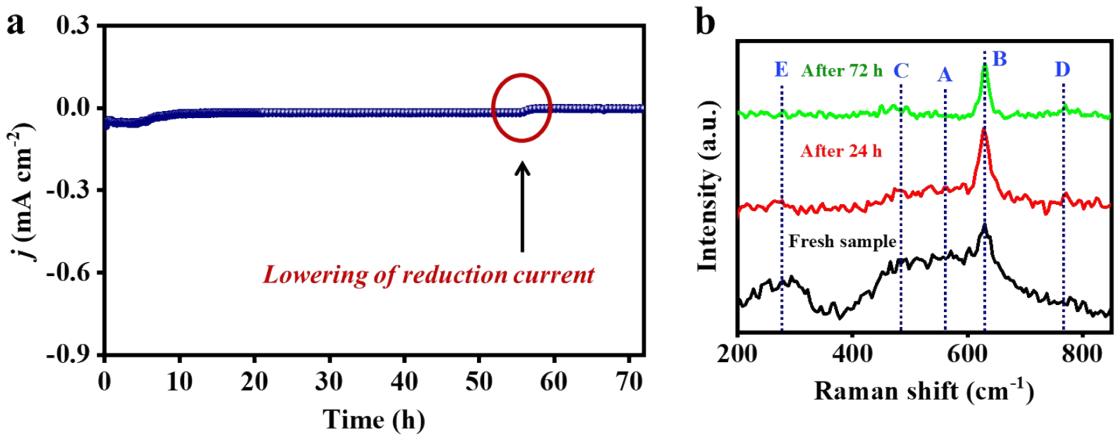

Fig. S37. (a) NRR stability experiment of SnO_2-600 catalyst at -0.3 V vs RHE for 72 h; (b) Raman spectra of the fresh sample compared with the post-stability samples after 24 and 72 h respectively.

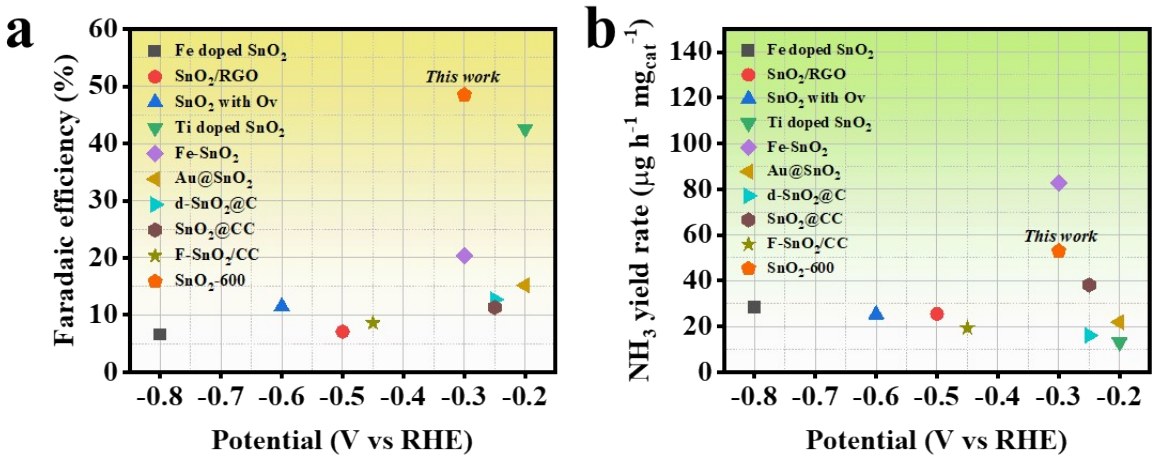

Fig. S38. (a, b) represent the Faradaic efficiency and NH_3 yield rate of our sample compared to all SnO_2-based reports on NRR respectively.

Table S1. Stabilization energy of the (101) plane of SnO_2 with bridge and in-plane oxygen vacancies calculated from DFT.

Vacancy Type	Removed Oxygen Percentage	DFT energy (eV)
Bridge Vacancy	1.39 %	-650.06
Bridge Vacancy	2.78 %	-642.85
In-plane Vacancy	1.39 %	-649.54
In-plane Vacancy	2.78 %	-640.60

From the table we can see that the DFT energy for bridge oxygen vacancy is higher than the DFT energy for in-plane oxygen vacancy. That means structure with bridge vacancy is more stable than that of in-plane vacancy.

Table S2. Crystallite size (L_c) determination of the (110) and (101) planes of all SnO_2 samples.

Material	(110) plane		(101) plane	
	2θ	Lc (nm)	2θ	Lc (nm)
SnO_2	26.97	3.28	34.16	3.94
SnO_2-500	26.92	5.96	34.12	6.25
SnO_2-600	26.76	9.27	34.05	8.47
SnO_2-700	26.74	16.12	34.02	14.32

Table S3. Percentage of bridge and in-plane oxygen vacancy density derived from deconvoluted Raman spectra of all samples.

Samples	SnO_2	SnO_2-500	SnO_2-600	SnO_2-700
% bo_v	25.97	55.06	57.64	59.25
% io_v	74.03	44.94	42.36	40.75

Table S4. Elemental atomic percentage of SnO_2-600 from EDAX and XPS analysis.

Elements	**Atomic % from EDAX**	**Sn:O**	**Atomic % from XPS**	**Sn:O**
Sn 3d	36.7	1:1.72	38.95	1:1.56
O 1s	63.3		61.05	

Table S5. Elemental atomic percentage of Sn^{4+} and Sn^{2+} in all samples from XPS Sn 3d narrow spectra.

Elements	**Atomic % of Sn^{4+}**	**Atomic % of Sn^{2+}**	**Sn^{4+}:Sn^{2+}**
SnO_2	97.35	2.65	1:0.027
SnO_2-500	97.08	3.02	1:0.031
SnO_2-600	96.75	3.26	1:0.034
SnO_2-700	96.52	3.48	1:0.036

Table S6. Positron annihilation lifetimes and intensities in all SnO_2 samples.

Sample	τ_1 (ps)	I_1 (%)	τ_2 (ps)	I_2 (%)	τ_{av} (ps)
SnO_2	-	-	383 ± 2	100 ± 1	383 ± 2
SnO_2-500	165 ± 22	6.6 ± 1.3	376 ± 2	93.4 ± 1.3	362 ± 6
SnO_2-600	162 ± 7	20.9 ± 1.4	359 ± 2	79.1 ± 1.4	318 ± 6
SnO_2-700	172 ± 4	46.9 ± 1.9	343 ± 4	53.1 ± 1.9	263 ± 7

Table S7. Quantitative analysis of purity of $^{14}N_2$ feed gas by colorimetric method.

	Source	NH_4^+ (μg mL^{-1})	NO_x (μg mL^{-1})	Total N content (μg mL^{-1})
$^{14}N_2$	Sigma Gases (99.9 % purity)	0.0004	0.0002	<0.001

Table S8. Comparative NRR experimental results for SnO_2-600 in 0.1 M Na_2SO_4 electrolyte.

Potential (V vs RHE)	Charge passed (C_p)	[NH_3] (μg mL^{-1})	Charge obtained (C_o)	Faradaic efficiency (%)	Yield rate (μg h^{-1} mg_{cat}^{-1})
-0.1	0.067	0.0367	0.014	20.8	26.8
-0.2	0.072	0.0527	0.020	27.7	28.8
-0.3	0.093	0.133	0.045	48.5	53.2
-0.4	0.107	0.1065	0.039	36.4	42.6
-0.5	0.110	0.0719	0.026	23.6	28.76

Table S9. Free energy calculation for the adsorption of N_2 and H at site A and site B of bridge-oxygen vacancy induced (101) oriented SnO_2.

(101) Oriented SnO_2			
Adsorption Type	**Free Energy (ΔG) at A site**	**Free Energy (ΔG) at B site**	**Remarks**
N_2	-0.28 eV		NRR Favorable Active Site
H	0.49 eV		
N_2		-0.13 eV	NRR Favorable Active Site
H		0.16 eV	
H adsorbed on oxygen atom		-1.25 eV	HER Favorable
** Because of bridge oxygen vacancies and poor oxygen on the surface, Sn atoms become pronounced active sites for H adsorptions, as reported in literature. But, from the table, we can see the change in free energy is more -ve in the case of N_2 adsorption as compared to H adsorption. So, the (101) oriented SnO_2 is more favourable for NRR.			

Table S10. Free energy calculation for the adsorption of N_2 and H at site C and site D of bridge-oxygen vacancy induced (110) oriented SnO_2.

(110) Oriented SnO_2			
Adsorption Type	**Free Energy (ΔG) at C site**	**Free Energy (ΔG) at D site**	**Remarks**
N_2	-0.10 eV		HER Favorable Active Site
H	-0.35 eV		
N_2		-0.27 eV	NRR Favorable Active Site
H		0.92 eV	
H adsorbed on oxygen atom		-0.84 eV	HER Favorable
**In the case of (110) oriented SnO_2 film, the vacancies of oxygen are less as compared to (101) oriented SnO_2 film. Therefore, O and Sn both are playing as active sites for H and N_2 adsorptions. At Sn site, near oxygen vacancy, the possibility of adsorption of H is more than N_2 adsorption. Also, the H adsorption on oxygen atoms occurs in an exothermic way. So, most of the H atoms are adsorbed on O and Sn atoms and results in HER.			

Table S11. NRR comparison for control samples at -0.3 V vs RHE.

Material	**Charge passed (C_p)**	**[NH_3] (μg mL^{-1})**	**Charge obtained (C_o)**	**Faradaic efficiency (%)**	**Yield rate (μg h^{-1} mg_{cat}^{-1})**
SnO_2	0.053	0.0389	0.013	24.9	15.56
SnO_2-500	0.081	0.0864	0.027	36.3	34.56
SnO_2-600	0.093	0.133	0.045	48.5	53.2
SnO_2-700	0.104	0.1283	0.043	42.01	51.32

Table S12. Comparative elemental atomic % of SnO_2-600 of fresh and after stability samples.

Elements	% Before stability	% After stability
EDAX		
Sn 3d	36.7	32.7
O 1s	63.3	67.3
XPS		
Sn 3d	38.95	33.95
O 1s	61.05	66.05
Deconvoluted O 1s peaks		
Lattice O	48.49	67.08
O-Vacancy	48.67	17.14
Chemisorbed O	2.85	15.78

Table S13. Literature comparison of SnO_2 based catalysts for NRR.

Catalyst	Electrolyte	Potential (V vs RHE)	Yield rate ($\mu g \cdot h^{-1} mg^{-1}_{cat}$)	Faradaic efficiency	Reference
Fe-doped SnO_2	0.1 M Na_2SO_4	-0.8 V	28.45	6.54 %	[2]
SnO_2/RGO	0.1 M Na_2SO_4	-0.5 V	25.6	7.1 %	[3]
SnO_2 with oxygen vacancy	0.1 M Na_2SO_4	-0.6 V	25.27	11.48 %	[4]
Ti doped SnO_2	0.1 M Na_2SO_4	-0.2 V	13.09	42.6 %	[5]
Janus Fe-SnO_2	0.1 M Na_2SO_4	-0.3 V	82.7	20.4	[6]
Au@amorphous SnO_2	0.1 M HCl	-0.2 V	21.9	15.2	[7]
d-SnO_2@C	0.1 M HCl	-0.25 V	16.68	12.7% at −0.15 V	[8]
SnO_2@CC	0.5M K_2SO_4	-0.25 V	38.18	11.33	[9]
F-SnO_2/CC	0.1 M Na_2SO_4	-0.45 V	19.3	8.6	[10]
SnO_2-600	**0.1 M Na_2SO_4**	**-0.3 V**	**53**	**48.5**	**This work**

Note: RGO- reduced graphene oxide, C- carbon, CC- carbon cloth.

References

1 X. Wang, J. Yang, M. Salla, S. Xi, Y. Yang, M. Li, F. Zhang, M. K. Zhu, S. Huang, S. Huang, Y. W. Zhang and Q. Wang, *Angewandte Chemie International Edition*, 2021, **60**, 18721–18727.

2 Y. Li, Y. Liu, X. Liu, Y. Liu, Y. Cheng, P. Zhang, P. Deng, J. Deng, Z. Kang and H. Li, *Nano Res*, 2022, **15**, 6026–6035.

3 K. Chu, Y. P. Liu, Y. B. Li, J. Wang and H. Zhang, *ACS Appl Mater Interfaces*, 2019, **11**, 31806–31815.

4 X. He, H. Guo, T. Liao, Y. Pu, L. Lai, Z. Wang and H. Tang, *Nanoscale*, 2021, **13**, 16307–16315.

5 Y. Yan, H. Qu, X. Zheng, K. Zhao, X. Li, Y. Yao and Y. Liu, *Chinese Chemical Letters*, 2022, **33**, 4655–4658.

6 L. Zhang, M. Cong, X. Ding, Y. Jin, F. Xu, Y. Wang, L. Chen and L. Zhang, *Angew Chem*, 2020, **132**, 10980–10985.

7 P. Wang, Y. Ji, Q. Shao, Y. Li and X. Huang, *Sci Bull (Beijing)*, 2020, **65**, 350–358.

8 G. Li, H. Jang, Z. Li, J. Wang, X. Ji, M. G. Kim, X. Liu and J. Cho, *Green Energy & Environment*, 2022, **7**, 672–679.

9 G. Li, Y. Yu, Z. Pan and L. An, *ACS Appl Energy Mater*, 2020, **3**, 6735–6742.

10 Y. P. Liu, Y. B. Li, H. Zhang and K. Chu, *Inorg Chem*, 2019, **58**, 10424–10431.